Hapres | Journal of Sustainability Research

sustainability.hapres.com

*Article*

# Flexible Operation and Control of Bidirectional Chargers Using ISMC for Electric Vehicle Applications

**Iman Soltani [1,*], Mohammad Reza Hasani [2], Farhad Shahnia [3,*]**

[1] Research Laboratory of Automotive Fluids and Structures Analysis, School of Automotive Engineering, Iran University of Science and Technology, Tehran 16846-13114, Iran

[2] Department of Electrical Engineering, Faculty of Engineering, University of Zanjan, Zanjan, 45371-38791, Iran; mrezahasani@znu.ac.ir (MRH)

[3] School of Engineering and Energy, Murdoch University, Murdoch, WA 6150, Australia

* Correspondence: Iman Soltani, Email: i_soltani@mail.iust.ac.ir; Farhad Shahnia, Email: F.Shahnia@murdoch.edu.au.

## ABSTRACT

The increasing integration of electric vehicles and renewable energy systems requires high-performance, reliable, and intelligent battery charging infrastructure. This paper presents a novel design and analysis of a bidirectional fast battery charging system connected to the power grid, employing a robust improved sliding mode control (ISMC) to overcome the limitations of conventional control methods. Conventional controllers such as PID, FL-PID, and ADRC suffer from parameter sensitivity, computational burden, and noise susceptibility under uncertain and dynamic conditions. In contrast, the proposed ISMC approach achieves improved robustness, fast dynamic response, and high tracking accuracy. The proposed architecture consists of two stages: a three-phase bidirectional voltage source converter on the AC side and a buck-boost DC/DC converter on the DC side. The voltage source converter employs the proposed ISMC to regulate the dq-axis grid currents and manage the active/reactive power flow, while the DC/DC converter is also governed by an ISMC approach to stabilize the DC-link and battery voltage across varying charge/discharge states. A significant contribution of this work is the proposed flexible operating algorithm that enables seamless transitions between grid-connected and islanded modes, ensuring uninterrupted supply to local AC and DC loads during grid outages through grid-forming control. Additionally, a battery management algorithm is integrated, which dynamically adjusts charging and discharging actions based on the battery's state of charge, thereby prolonging battery lifespan and ensuring safe operation. Verifications via simulations in MATLAB/Simulink confirm the superiority of the proposed control strategy by demonstrating less than 3% total harmonic distortion in grid current, accurate current tracking, and a stable DC voltage profile with negligible overshoot and fast settling time. In comparison, the PI controller

**Open Access**

Received: 12 Jan 2026
Accepted: 05 Mar 2026
Published: 09 Mar 2026

exhibits 0.4% overshoot and 50 ms settling time, while the ADRC shows about 0.3% overshoot and 40 ms settling time. The ISMC-based framework can be applied to next-generation smart battery charging stations, providing enhanced grid support, improved power quality, and advanced battery health management.

**KEYWORDS**: sliding mode control; bidirectional converter; fast battery charger; V2G/G2V; battery management

## ABBREVIATIONS

ADRC, Active disturbance rejection control; BMS, Battery management system; CB, Circuit breaker; CC, Current charging mode; CV, Voltage charging mode; dq, Direct/quadrature; ESS, Energy storage system; EV, Electric vehicle; E2G, ESS-to-grid; E2L, ESS-to-load; GFL, Grid-following mode; GFM, Grid-forming mode; G2E, Grid-to-ESS; G2V, Grid-to-vehicle; HCC, Hysteresis current controller; IGBT, Insulated gate bipolar transistor; ISMC, Improved sliding mode control; MPC, Model predictive control; PCC, Point of common coupling; PLL, Phase-locked loop; PV, Photovoltaic; PWM, Pulse-width modulation; SMC, Sliding mode control; SOC, State of charge; THD, Total harmonic distortion; VSC, Voltage source converter; V2G, Vehicle-to-grid

## INTRODUCTION

### Background and Motivation

The widespread deployment of electric vehicles and renewable energy sources has intensified the need for efficient and reliable power conversion infrastructures. As energy systems become more dynamic and decentralized, the demand for reliable and efficient battery charging infrastructures continues to rise. Traditional power systems are evolving toward more flexible and interactive networks where energy flow is not unidirectional. This shift calls for charging systems that can adapt to changing grid conditions and support bidirectional energy exchange [1,2]. Effective control of power converters in such systems is essential to ensure stable operation and superior performance. However, modern power electronics systems are often affected by nonlinear behavior, load variability, and parameter uncertainty. These factors can compromise the accuracy and robustness of conventional control methods. Therefore, control strategies that can handle such complexities are increasingly required. Ensuring high power quality, reducing losses, and maintaining system stability are key goals in the design of next-generation charging systems. Furthermore, managing the charging process in a way that protects the battery and prolongs its life is an essential consideration in practical applications. These challenges drive ongoing research into control and design strategies for advanced grid-connected battery chargers [3,4]. Sliding mode control (SMC) offers strong robustness against

system nonlinearities, parameter uncertainties, and load variations, making it well-suited for grid-connected battery charger control. Unlike conventional linear controllers, SMC maintains stable and accurate performance under disturbed or poorly modeled conditions while providing fast dynamic response and inherent disturbance rejection.

**Literature Review**

In recent years, the growing electrification of transportation and increasing deployment of renewable energy systems have brought about a critical demand for advanced battery charging infrastructure. As electric vehicles (EVs) and energy storage systems (ESSs) become central to smart grid evolution, bidirectional battery chargers are gaining prominence. These systems not only charge the battery (grid-to-vehicle or G2V) but also allow power to flow back to the grid (vehicle-to-grid or V2G), playing a vital role in peak shaving, load balancing, and ancillary services [1–4].

Bidirectional charging demands converters that are both efficient and versatile, capable of maintaining high performance under fast-changing load and grid conditions. Among the many converter structures, isolated topologies such as dual-active bridge converters have received extensive attention due to their galvanic isolation and soft-switching capability. Recent developments have focused on enhancing the DAB performance under wide voltage variations. A study demonstrated a single-phase-shift controlled DAB achieving zero-voltage switching across a broad operating range, improving efficiency and reducing electromagnetic interference [5]. Another work involving a 3.5 kW soft-switching DAB-based on-board charger integrated with an AC side LCL filter achieved low total harmonic distortion (THD) and high-power factor through direct/quadrature (dq) axis current control [6].

In parallel, non-isolated converters like bidirectional buck–boost and SEPIC topologies have also appeared as practical candidates for fast battery charging, especially in lower voltage applications. These simpler, more compact, and cost-effective structures were highlighted in a study on a multifunctional bidirectional SEPIC converter coupled with a VSC and photovoltaic (PV) system, which operated effectively under both island and grid-connected conditions with THD below 5% [7]. Buck–boost converters with automated mode selection have proven practical for integrated PV–battery systems [8]. A flyback-based bidirectional charger using SMC was proposed in [9], achieving stable voltage regulation and good dynamic response under grid disturbances.

Control strategies are critical in managing bidirectional power flow. Although conventional PI controllers are still in use, research has increasingly focused on advanced techniques like SMC, model predictive control (MPC), active disturbance rejection control (ADRC), and machine learning–based methods. SMC-based approaches show strong resilience to external disturbances and model inaccuracies. A comparative study between conventional SMC and ISMC on DC-DC converters concluded that

ISMC offers superior current tracking and smoother control [10]. An implementation of double-integral SMC combined with phase-shift modulation in bridgeless interleaved converters resulted in fast dynamic response and zero-voltage switching [11]. Sliding-mode current control has also proven effective in high-power bidirectional chargers, enabling precise battery current tracking under varying charging conditions [12].

The MPC strategy offers another promising alternative by predicting system behavior over a time horizon. A study applied MPC to synchronous boost converters in V2G applications, delivering faster convergence and better load following than classical controllers [13]. In [14], ADRC was used in a fast DC charging scenario, proving its ability to suppress disturbances without relying on precise modeling.

Coordination of multiple power flows—especially in grid, renewable, and EV-connected systems—demands more advanced strategies. Droop control, traditionally used for microgrid power sharing, has been adapted for bidirectional chargers. A study introduced a 3D droop control mechanism to align AC and DC power references for grid stability and reactive power compensation [15]. Adaptive current control schemes with phase-shift algorithms have also emerged to enhance grid-following capabilities in bridgeless charger front-ends [16].

Refinements to classical PI control persist. An investigation of nonlinear PID tuning in bidirectional buck–boost converters demonstrated improved system stability and transient response [17]. Certain works have integrated machine learning, such as a neural network–based voltage regulator using dual heuristic programming to outperform PI controllers under nonlinear conditions [18].

As power electronics evolve, multifunctional integration with solar PV and energy storage becomes essential. A design featuring a SEPIC–VSC hybrid charger linked to both grid and PV sources smoothly transitioned between G2V and V2G modes, supported by a synchronous reference frame phase-locked loop (PLL) and a second-order generalized integrator for grid synchronization and power quality [7].

Wireless bidirectional charging is gaining attention. Although it lags wired systems, recent work has examined control of wireless energy transfer using phase-shift modulation and frequency tuning. A review highlighted challenges such as coil misalignment and reactive power control while suggesting four-quadrant regulation techniques [19]. Several comprehensive reviews published in 2024–2025 have consolidated the state of the art. One analytical survey detailed converter topology (multilevel, dual active bridge, partial power converters) and control strategies (PI, MPC, and ML), mapping trade-offs between complexity, efficiency, harmonics, and robustness [20]. Another study focused on partial power converters and their role in ultra-fast charging, emphasizing their compact size and specialized handling of high-power charging paths [4].

These developments reveal a notable trend: bidirectional chargers have evolved from simple converters into intelligent energy nodes equipped with adaptive, predictive, and robust control. They not only manage power flow but also adapt to grid conditions, battery health, and environmental factors. Integration of battery management is evident, with embedded state of charge (SOC) estimation and lifecycle optimization. Battery thermal studies and related thermal limitations will be considered in future work. A comparative overview of the stated control methods for EV chargers has been listed in Table 1.

**Table 1.** Comparative overview of control strategies in EV charging systems.

| Ref. | System/ Application | Control Method | Grid Mode | Merits | Limitations | Relevance to EV Chargers |
|---|---|---|---|---|---|---|
| [2] | Bidirectional low-voltage EV charger | PI-based control | GFM* | Simple implementation, proven topology | Weak robustness to nonlinearities & disturbances | On-board/off-board low-voltage EV chargers |
| [5] | 350 kW DC fast charger dual active bridge | Phase-shift modulation + PI loops | GFM | Ultra-high efficiency, optimized magnetics | Focus on modulation not robust control; no GM | Public ultra-fast DC stations |
| [8] | 6.6 kW high-frequency dual active bridge charger | Single phase shift + PI | GFM | Soft-switching, compact design | Limited transient robustness; simple regulation | On-board or slow DC charging |
| [9] | PV + grid-connected EV charger | MPPT + PI current control | GFM | G2V & V2G capability, hybrid sources | No nonlinear robust control; grid-dependent | Renewable-assisted charging stations |
| [10] | Interleaved dual active bridge charger | PI loops + current balancing | GFM | Reduced ripple, high power density | PI tuning is sensitive to uncertainties | Fast EV charging DC stage |
| [12] | 3-phase PV-integrated charger | PLL + PI regulation | GFM | Coordinated RES & grid charging | Cannot operate in islanded mode | Station-level chargers with PV |
| [13] | SiC-based dual active bridge charger | PI + modulation | GFM | Higher efficiency via SiC switching | Still linear control; robustness not addressed | Compact fast EV chargers |
| [14] | Multiport PV–EV DC system | Energy management + PI loops | GFM | High functional integration | No strong disturbance rejection | Hybrid solar EV stations |
| [16] | Low-voltage bidirectional charger | PI controller | GFM | Hardware validated; bidirectional operation | No uncertainty compensation | Small vehicle/ scooter chargers |
| [18] | Fast charger with station BESS | Optimized state-space / PI loops | GFM | Peak shaving & efficiency optimization | Complex tuning; no GM | Hub-scale DC charging |
| [21] | Fast DC charger G2V/V2G | ADRC control | quasi-GFM | Disturbance rejection, multifunction operation | Tuning complexity; noise sensitivity | Advanced Battery EV fast charging |
| [3,7] | Review of V2G chargers | Mostly PI & MPC; few SMC cases | Mostly GFM | Comprehensive literature surveys | Highlights absence of robust & GM controllers | Identifies a gap for advanced EV charger control |
| Proposed | Bidirectional Fast charger G2V/V2G | ISMC & charge management | GFM-GFL# | Accurate tracking voltages and currents- power management | Potential distortion during transition from GFL to GFM | ultra-fast DC stations |

*GFM: Grid-forming mode, #GFL: Grid-following mode.

**Novelties and Contributions**

The literature review reveals that existing control methods for bidirectional chargers have notable limitations. Conventional PID, FL-PID, and ADRC controllers each face challenges under disturbances and uncertainties. For example, conventional PID controllers often struggle in the presence of system uncertainties and require frequent manual retuning. Meanwhile, FL-PID controllers, due to their reliance on expert-defined rules, tend to exhibit sluggish transient responses. Despite their ability to reject external disturbances under uncertain conditions, ADRC controllers have drawbacks such as tuning complexity and sensitivity to noise. In contrast, the SMC method can rapidly and effectively manage disturbances in the presence of various system uncertainties. Moreover, the SMC method ensures system stability under both transient and steady-state conditions, thereby overcoming the limitations of conventional control approaches. While SMC inherently involves the chattering phenomenon, it can be significantly mitigated through the implementation of effective techniques.

In this paper, a bidirectional grid-connected battery charging system based on a robust ISMC is proposed. In the proposed architecture, both the AC/DC and DC/DC converters are controlled using the ISMC method. With this approach, both converters are bidirectional and capable of not only charging and discharging the battery but also efficiently supplying local DC and AC loads. Therefore, under conditions where the power grid is interrupted, the AC/DC converter must operate in grid-forming mode to ensure continued supply to the AC side loads from the battery bank. A charge management algorithm is proposed to regulate the DC-link voltage and battery power, enabling dynamic control of charging and discharging operations based on the battery's SOC. The bidirectional power flow in the proposed fast battery charging system is illustrated in Figure 1. As shown, three modes of energy flow management are considered: In Mode 1, as shown in Figure 1a, the three-phase distribution grid supplies both the AC and DC loads, while also charging the ESS. In Mode 2, according to Figure 1b, the direction of power flow in the bidirectional charging system is reversed. Under these conditions, the ESS—depending on its SOC—can supply power to both AC and DC loads. If there is surplus energy in the ESS, it will be exported to the utility grid. In Mode 3, considering Figure 1c, if the grid is completely disconnected, the ESS must supply both AC and DC loads independently. In this case, the bidirectional converter must operate in grid-forming mode to effectively control the voltage and frequency of the AC side loads.

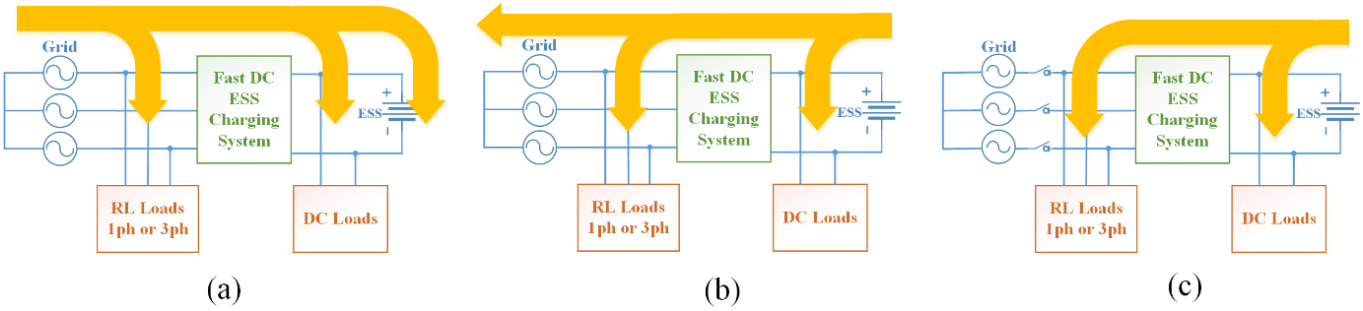


**Figure 1.** Bidirectional power flow in fast DC charging system, (**a**) Grid to ESS (G2E), (**b**) ESS to Grid (E2G), (**c**) ESS to Loads (E2L).

This work introduces the following methodological innovations, aimed at addressing the limitations of conventional control strategies (e.g., PI, ADRC, and classic SMC) in bidirectional electric-vehicle battery chargers under nonlinear dynamics and parametric uncertainties:

1. Novel sliding surface design: A new integral sliding surface is developed that simultaneously incorporates DC-link voltage regulation and active power tracking objectives. Unlike conventional design methods, the proposed design enables coordinated control of energy flow and voltage stability, resulting in improved transient behavior and reduced sensitivity to grid disturbances and load variations.
2. Innovative SMC-based controller for the DC/DC converters: An ISMC-based controller is implemented directly for the non-isolated DC/DC converter, generating reference control signals for the hysteresis current controller (HCC) without relying on intermediate linear controllers or conventional phase-shift modulation schemes. This enables robust operation over wide variations in battery voltage and load conditions while preserving stability and fast dynamic response.
3. Unified power management structure: A novel power management framework based on ISMC is proposed to coordinate G2E, E2G, and E2L operating modes within a single control architecture. In contrast to traditional supervisory control or rule-based mode switching methods, the proposed approach ensures smooth transitions between charging and discharging states without requiring multiple dedicated controllers or complex scheduling layers.
4. Integration of droop control with ISMC for dual grid operation: For the first time in this context, droop control is integrated directly into the ISMC framework to enable seamless dual-mode operation in both grid-following and grid-forming controllers. This hybrid strategy allows the charger to provide voltage–frequency support during islanded operation while maintaining synchronized grid-following performance under grid-connected conditions, addressing a critical functional gap in the existing EV charger control schemes.

Despite the significant progress reported in the literature, several limitations remain, including sensitivity to parameter uncertainties, degraded dynamic performance under operating condition changes, and limited robustness during mode transitions between grid-following and grid-forming operation. In addition, many existing approaches rely on linear control structures that require extensive tuning and may exhibit reduced performance under disturbances and modeling inaccuracies. To address these challenges, this paper proposes the ISMC strategy with enhanced robustness against parameter variations and external disturbances while maintaining fast transient response. By integrating the ISMC framework into the grid-interactive control architecture, the proposed approach effectively overcomes the identified limitations and provides stable operation across different modes and operating conditions.

## OVERALL CONFIGURATION OF BIDIRECTIONAL FAST CHARGERS

The overall architecture and configuration of the proposed ISMC based grid-connected bidirectional fast-charging system is illustrated in Figure 2. This system consists of two stages: an AC/DC converter and a DC/DC converter, and is designed to manage bidirectional power flow for supplying loads and charging the battery. When the fast-charging system is connected to the power grid via a circuit breaker (CB) and a first-order RL filter, the bidirectional AC/DC converter operates in grid-following mode, ensuring frequency synchronization between the grid and the converter, while executing power transfer in accordance with a dedicated power management algorithm. In case of a complete grid outage, the ESS must supply both the DC and AC loads. Under this condition, the AC/DC converter switches to grid-forming mode to regulate the voltage and frequency of the AC loads accurately. The AC side loads can be modeled as single-phase or three-phase RL parallel circuits. On the DC side, the total load is represented by a resistor R_L in parallel with the DC-link capacitor. The bidirectional buck-boost DC/DC converter is responsible for managing power flow between the ESS and the grid and regulating the ESS voltage accordingly.

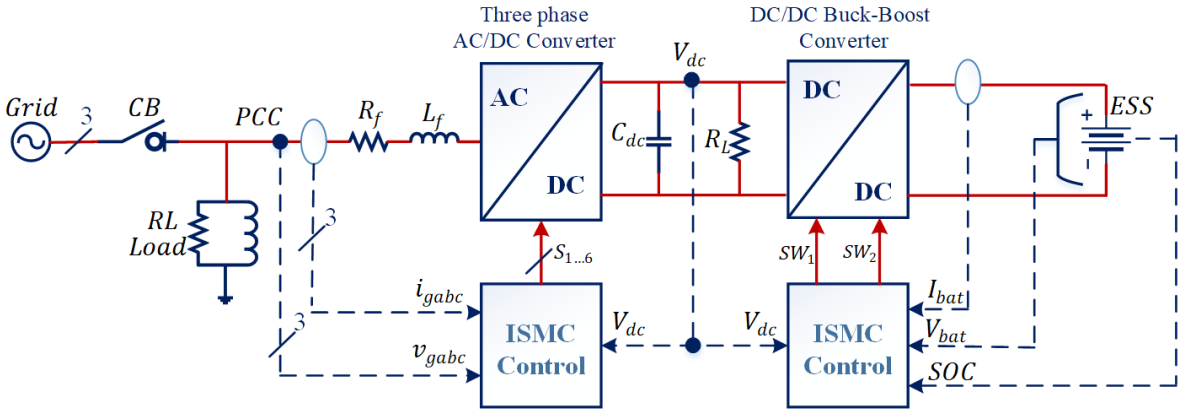


**Figure 2.** Overall architecture of bidirectional fast-charging system based on ISMC.

Both AC/DC and DC/DC converters are effectively controlled using a robust ISMC, providing robustness against system uncertainties and modeling inaccuracies. These controllers ensure precise and rapid tracking of the DC-link voltage and three-phase grid currents, delivering a desirable dynamic response even under voltage and power disturbances. The integrated operation of the proposed fast-charging system requires an effective power management strategy to ensure safe and reliable power delivery to the connected loads. Figure 3 illustrates the energy flow within the proposed charging system and its interactions among key components. Residential AC and DC loads can be reliably and safely powered by either the utility grid or the ESS, depending on the implemented power management algorithm within the control framework.

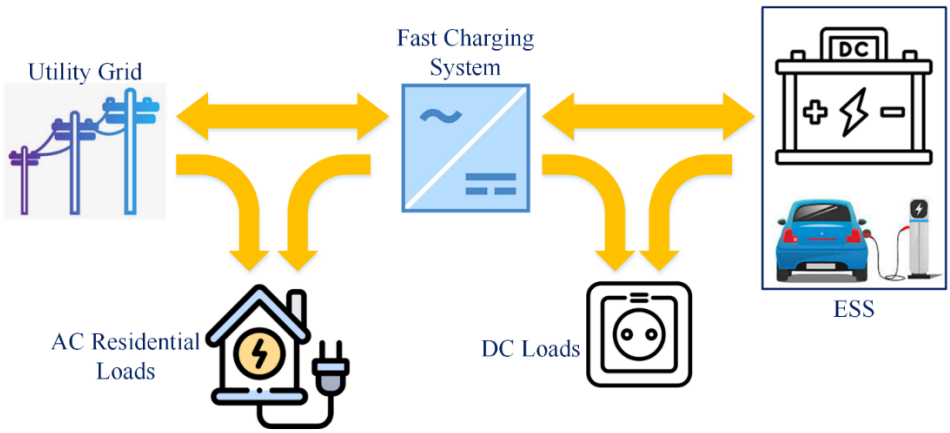


**Figure 3.** Energy flow within the proposed fast DC charging system.

When the fast-charging system is connected to the power grid, the priority is to supply the system loads and charge the ESS. If the ESS is fully charged, it will not discharge as long as the charging system remains connected to the grid, unless the power drawn from the grid is limited due to grid code requirements or peak shaving constraints. In such cases, the system loads will be supplied jointly by the grid and the ESS. In case of a grid outage caused by faults or unforeseen incidents, the ESS must switch to discharge mode to supply the system loads. Therefore, maintaining a fully charged ESS is essential for ensuring system reliability during critical or emergency conditions.

### Modeling of DC/DC Bidirectional Converter

To regulate the battery voltage and power, a bidirectional buck-boost DC/DC converter is employed, consisting of two switches, a capacitor ($C_{bat}$), and an inductor ($L_{bat}$), as shown in Figure 4. This converter connects the ESS to the DC-link and ensures energy balance during different operating modes: G2E, E2G, and E2L. The insulated gate bipolar transistor (IGBT) switches, driven by complementary control signals, enable bidirectional current flow through the converter. By precisely controlling the duty cycle, the converter can regulate the switching sequence such that the output

voltage becomes either higher or lower than the input voltage, depending on the system requirements. It should be pointed out that the modeling of switching losses is not the focus of this paper.

In the ESS charging mode (i.e., G2E), the DC/DC converter operates in buck mode to effectively step down the DC-link voltage to the required battery charging voltage. In the discharging mode (i.e., E2G and E2L), the converter operates in boost mode to step up the battery voltage for delivering power to the utility grid or household loads, thereby aligning it with the DC-link voltage. The parameters $L_{bat}$ and $C_{bat}$ can be calculated using (1) and (2), respectively [21].

$$L_{bat} = \frac{V_{dc} - V_{bat}}{2\Delta i_L f_s} \tag{1}$$

$$C_{bat} = \frac{\Delta i_L}{8\Delta v_c i_L f_s} \tag{2}$$

where $V_{dc}$ is the DC-link voltage, $V_{bat}$ is the ESS voltage, $\Delta i_L$ is the allowable current ripple of the inductor $L_{bat}$, and $\Delta v_c$ is the allowable voltage ripple of the capacitor $C_{bat}$. $f_s$ represents the switching frequency of the DC/DC converter.

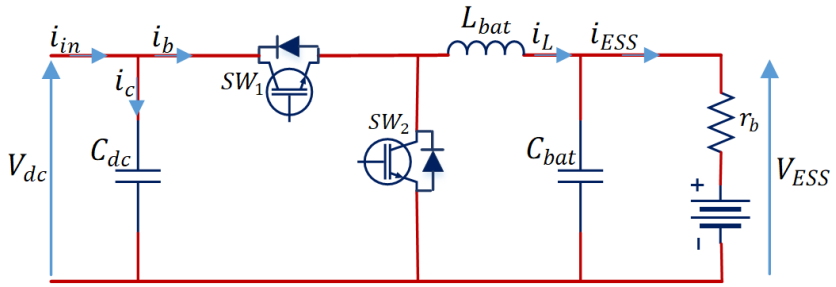


**Figure 4.** Circuitry diagram of the DC/DC buck-boost converter.

The state-space equations of the bidirectional buck-boost DC/DC converter, as shown in Figure 4, are presented as:

$$\frac{dV_{dc}}{dt} = \frac{1}{C_{dc}}(i_{in} - i_b) \tag{3}$$

$$\frac{dV_{ESS}}{dt} = \frac{1}{C_{bat}}(i_L - i_{ESS}) \tag{4}$$

$$\frac{di_{ESS}}{dt} = \frac{1}{L_{bat}}(g.V_{dc} - V_{ESS}) \tag{5}$$

where $i_{in}$ represents the input current drawn from the grid, $i_b$ is the output current of DC capacitor ($C_{dc}$), $i_L$ is the inductor current $L_{bat}$, $i_{ESS}$ denotes the battery current, $V_{ESS}$ is the battery voltage, and $g$ is the gain of the boost converter.

Therefore, the state-space representation derived from the above equations is given by:

$$\begin{bmatrix} \dot{V}_{dc}(t) \\ \dot{V}_{ESS}(t) \\ i_{ESS}\ (t) \end{bmatrix} = \begin{bmatrix} \frac{1}{C_{dc}} & 0 & 0 \\ 0 & 0 & \frac{1}{C_{bat}} \\ \frac{g}{L_{bat}} & -\frac{1}{L_{bat}} & 0 \end{bmatrix} \begin{bmatrix} V_{dc}(t) \\ V_{ESS}(t) \\ i_{ESS}(t) \end{bmatrix} + \begin{bmatrix} -\frac{1}{C_{dc}} \\ 0 \\ 0 \end{bmatrix} i_{in} \quad (6)$$

**Modeling of AC/DC Bidirectional Converter**

In this section, the modeling of the bidirectional AC/DC converter is presented for the management and control of power conversion between the DC-link and the power grid. As previously mentioned, when the fast-charging system is connected to the power grid (i.e., during G2E and E2G modes), the AC/DC converter will run in grid-following mode to achieve voltage and frequency synchronization with the grid [22]. To filter out high-frequency noise, a first-order RL filter is employed to ensure that the power delivered to or received from the grid is smooth, distortion-free, and of high-power quality. During the discharge mode (i.e., E2L) and in case of a grid disconnection, the AC/DC converter must operate in grid-forming mode to establish a stable local grid for supplying residential AC loads. The grid-connected bidirectional AC/DC converter along with the RL filter is illustrated in Figure 5.

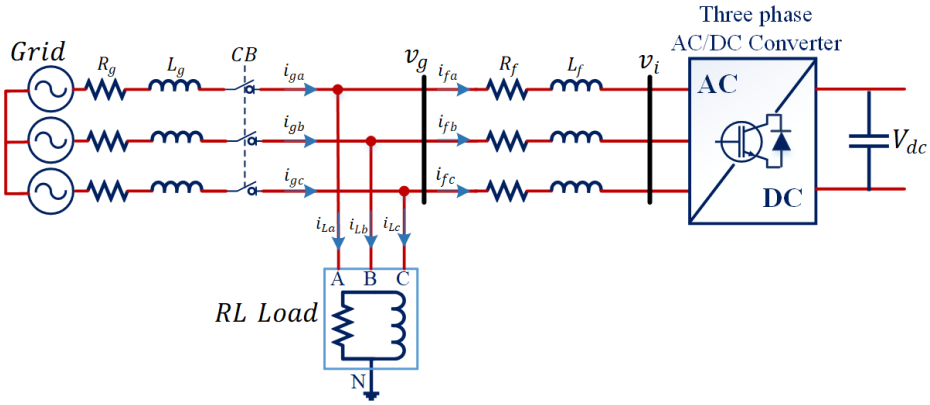


**Figure 5.** Structure of the AC/DC bidirectional converter connected to grid.

Accordingly, the AC side voltage-current equations of the converter in the three-phase *abc* reference frame are expressed by:

$$v_{g_k} = v_{i_k} - R_f i_{f_k} - L_f \frac{di_{f_k}}{dt}, \qquad \forall k \in a, b, c \quad (7)$$

In (7), *a*, *b*, and *c* represent each phase of the three-phase system. $R_f$ and $L_f$ denote the resistance and inductance of the RL filter, respectively. $v_{g_k}$ and $v_{i_k}$ refer to the phase voltages at the point of common coupling (PCC) and the converter terminals, respectively. $i_{f_k}$ represents the three-phase converter currents.

In the synchronous *dq* reference frame, the above voltage-current equations are expressed as:

$$L_f \frac{di_{fd}}{dt} = v_{id} - v_{gd} - R_f i_{fd} - L_f \omega_g i_{fq} \quad (8)$$

$$L_f \frac{di_{fq}}{dt} = v_{iq} - v_{gq} - R_f i_{fq} + L_f \omega_g i_{fd} \quad (9)$$

where, $v_{id}$ and $v_{iq}$ are the converter terminal voltage components in the synchronous dq reference frame, $v_{gd}$ and $v_{gq}$ are the grid voltage components, and $i_{fd}$ and $i_{fq}$ are the converter current components, all expressed in the synchronous *dq* reference frame. In grid-following mode, the converter synchronizes to the grid voltage through a PLL and regulates the injected current based on grid voltage references. In contrast, in grid-forming mode, the converter runs as a controlled voltage source, establishing its own voltage magnitude and frequency references without relying on grid synchronization. The transition between grid-following and grid-forming modes is achieved by smoothly reconfiguring the outer control loop, while the inner current control structure remains unchanged.

## PROPOSED ISMC-BASED CONTROLLERS FOR THE DC/DC CONVERTER

The bidirectional DC/DC converter controls the power flow between the grid, the ESS, and the system loads. Therefore, an ISMC-based strategy is proposed for managing energy flow for G2E, E2G and E2L operating modes. This proposed control strategy, illustrated in Figure 6, operates according to the following logic:

- In grid-connected mode, the reference current is calculated by dividing the reference power ($P^*_{G2E}$ or $P^*_{E2G}$) by the ESS voltage. The ISMC then processes the control error $\Delta I_{ESS}$ and sends it to a hysteresis band controller to generate the switching pulses for the DC/DC converter.
- When the SOC of the ESS reaches above 80%, the ESS charge mode selection algorithm switches to CV mode as shown in Figure 6. The ISMC is used to regulate the battery voltage, ensuring that the batteries are charged with a lower current.
- Upon disconnection from the main grid, the mode selection algorithm transitions to E2L mode. In this condition, the ISMC regulates the DC-link voltage $V_{dc}$ by generating the desired reference current $i^*_{E2L}$, thereby ensuring reliable power delivery to local AC and DC loads.

Figure 7 shows the supervisory mode selection scheme used to control ESS charging and discharging through the bidirectional DC/DC converter. The selection of the ESS charging and discharging modes depends on the grid connection status and the SOC of the batteries. When the fast-charging system is connected to the grid, the grid current (i_g) is non-zero, and the DC/DC converter can operate in CC_E2G, CC_G2E, or CV_G2E modes. Otherwise, in the absence of grid current, the DC/DC converter operates in E2L mode to maintain DC-link voltage regulation, allowing the ESS to support the system loads.

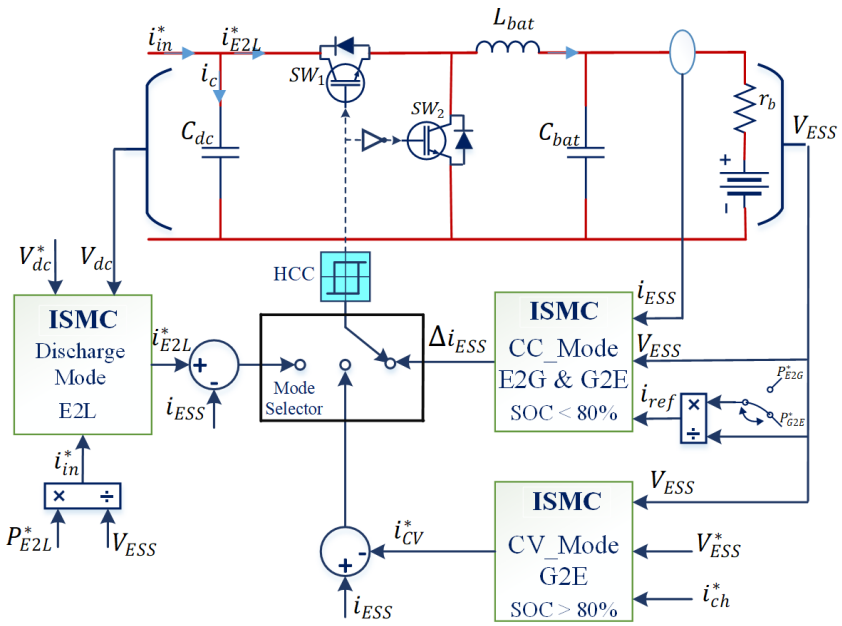


**Figure 6.** Control of the DC/DC bidirectional converter based on the ISMC method.

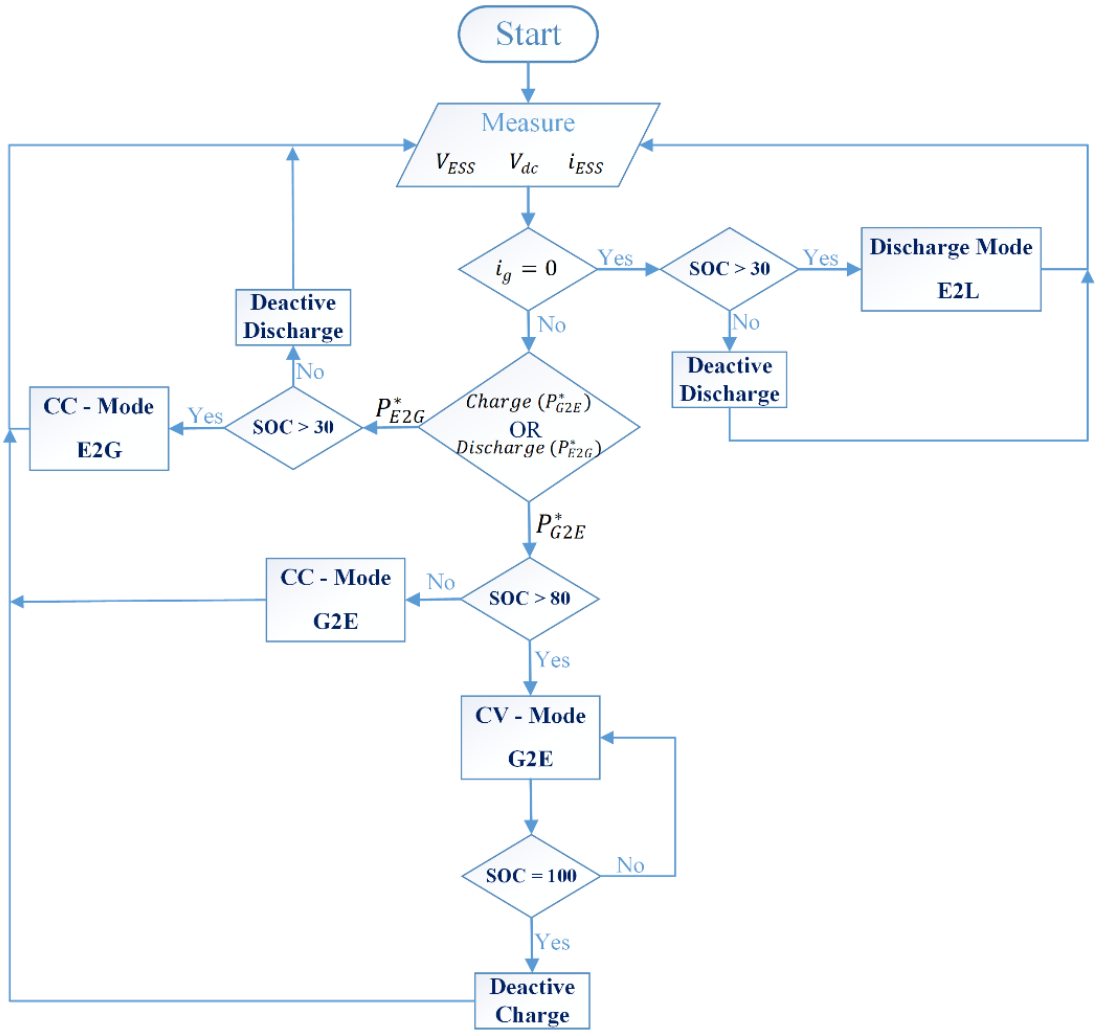


**Figure 7.** Flowchart of modes activation for managing DC/DC converter.

If the SOC of the ESS falls below 30% (discharge threshold), the discharging process will stop to preserve the battery's health. Similarly, when the SOC reaches 80% during charging, the proposed algorithm transitions from CC mode to CV mode, allowing the battery to charge with a reduced current. Finally, when the SOC reaches 100% (stop charging) in CV mode, the charging process must be stopped to ensure battery safety and longevity. The SOC is assumed to be provided by an external battery management system (BMS) using a standard estimation approach based on coulomb counting with periodic voltage-based correction. Such methods are widely adopted in practical battery systems and provide sufficiently accurate SOC information for supervisory charging and discharging decisions. It should be noted that while such threshold-based logic is sufficient to demonstrate the feasibility of the proposed grid-following/grid-forming control framework, more advanced BMS strategies—incorporating thermal constraints, aging-aware limits, and adaptive SOC thresholds—may be more suitable for real-world deployment.

**Designing ISMC for Discharging Mode (E2L)**

To ensure precise tracking of the DC-link voltage ($V_{dc}$) relative to its reference value ($V_{dc}^{*}$), ISMC is designed for the DC/DC bidirectional buck-boost converter associated with the ESS. The objective of the ISMC design is to drive the system state trajectories toward the desired sliding surface in an exponential manner and ultimately converge to the system equilibrium point (i.e., the reference voltage). The reference discharge current ($i_{in}^{*}$) is obtained through reference E2L power ($P_{E2L}^{*}$) divided by $V_{ESS}$. As is well known, the state-space equations of a linear time-invariant system are represented by:

$$\dot{x} = Ax + Bu \tag{10}$$

Therefore, the state-space equation for the DC bus voltage of the fast-charging system is expressed by (11) through simplifying (3).

$$\dot{V}_{dc} = \frac{1}{C_{dc}} i_{in} - \frac{1}{C_{dc}} i_b \tag{11}$$

where $i_b$ represents the DC/DC converter current, $i_{in}$ denotes the input current drawn from the grid. To enhance clarity in the ISMC design, a variable transformation is applied to (11), and it is subsequently rewritten as:

$$\dot{x} = f + u \tag{12}$$

where:

$$x = V_{dc} \tag{13}$$

$$f = \frac{1}{C_{dc}} i_{in} \tag{14}$$

$$u = -\frac{1}{C_{dc}} i_b \tag{15}$$

An integral sliding surface ($s$) can be proposed as:

$$s = \tilde{x} + \lambda \int \tilde{x}\, dt \tag{16}$$

where $\lambda_1$ is a strictly positive constant, $\tilde{x}$ defines the control error for state variable of $x$, and it is given by:

$$\tilde{x} = x - x_d \tag{17}$$

in which $x_d$ is the desire value of the state variable of $x$. To ensure stable sliding conditions, a positive definite Lyapunov function is defined as:

$$V(s) = \frac{1}{2} s^2 \tag{18}$$

To ensure exponential convergence to the sliding surface and the reference values, the following condition must be satisfied:

$$\dot{V}(s) \leq -\eta |s| \;\Rightarrow s\dot{s} \leq -\eta |s| \tag{19}$$

where $\eta$ is a positive constant. In order to design ISMC, at first, the derivative of $s$ in the (16) ($\dot{s}$) must be calculated.

$$\dot{s} = \dot{\tilde{x}} + \lambda_1 \tilde{x} = \dot{x} - \dot{x}_d + \lambda_1 \tilde{x} \tag{20}$$

Substituting (12) in (20), and then setting $\dot{s} = 0$, the equivalent input ($\hat{u}_{eq}$) is obtained as:

$$\hat{u}_{eq} = -\hat{f} + \dot{x}_d - \lambda_1 \tilde{x} \tag{21}$$

where $\hat{f}$ denotes the estimated function of $f$, which considering (14), it is chosen as:

$$\hat{f} = \frac{k_1}{C_{dc}} i_{in} \tag{22}$$

where $0 < k_1 < 1$. The constants ($k_1, \lambda_1, \eta_1$) are typically chosen based on the constraints and limitations of the problem, as well as the performance of the simulation outputs.

The ultimate control action ($u$) is achieved by (23) due to (21).

$$u = \hat{u}_{eq} - ksign(s) \tag{23}$$

where $k$ is a design constant determined based on the sliding conditions. To mitigate the chattering phenomenon, a redesign is necessary. For this purpose, the function provided in (24) is utilized instead of the sign function.

$$\Psi(s) = \frac{s}{|s| + \varphi} \tag{24}$$

which $\varphi$ represents the chattering band. Thus, the Equation (23) can be rewritten as:

$$u = \hat{u}_{eq} - k\Psi(s) \tag{25}$$

To achieve sliding conditions with exponential convergence as defined in (19), the expression $s\dot{s}$ must be derived. By substituting (12) and (23) into (20) and multiplying it by 's', we obtain:

$$\begin{aligned} s\dot{s} &\leq s\left(f - \hat{f} - ksign(s)\right) \\ s\dot{s} &\leq s\left(f - \hat{f} - k\frac{|s|}{s}\right) \\ s\dot{s} &\leq |s| \underbrace{\left|f - \hat{f}\right|}_{\hat{F}} - k|s| \\ s\dot{s} &\leq |s| \underbrace{(\hat{F} - k)}_{-\eta} \end{aligned} \tag{26}$$

Based on (26), the exponential sliding condition are derived as:

$$k \geq F + \eta \tag{27}$$

Which the function $F$ can be obtained as:

$$\begin{gathered} \left|f - \hat{f}\right| \leq \left|\frac{1}{C_{dc}} i_{in} - \frac{k_1}{C_{dc}} i_{in}\right| \leq \frac{1 - k_1}{C_{dc}} |i_{in}| \\ F \triangleq \frac{|1 - k_1|}{C_{dc}} |i_{in}| \end{gathered} \tag{28}$$

By substituting (13)–(15) into (21), then replacing (21) in (23), the general control law is obtained based on the actual system parameters.

$$i_{E2L}^{*} = k_1 i_{in} - C_{dc}\dot{V}_{dc,ref} + C_{dc}\lambda_1 \tilde{V}_{dc} + (C_{dc}\eta + (1 - k_1)|i_{in}|)sign(s) \tag{29}$$

The reference signal generated for the DC/DC converter in the E2L based on ISMC ($i_{E2L}^{*}$) is compared with the ESS output current ($i_{ESS}$), as illustrated in Fig6. The resulting error signal is then fed into the HCC block, which generates the switching pulses for the DC/DC bidirectional buck-boost converter.

**Designing ISMC for CV Charging Mode (G2E)**

When the SOC of the ESS reaches 80%, the CV charging mode (G2E) is activated so that the batteries are charged with a lower current. The ISMC is designed in this mode to accurately track the ESS voltage. Therefore, the state-space equation of (4) is used for controller design and is rewritten as:

$$\dot{V}_{ESS} = \frac{1}{C_{bat}} i_L - \frac{1}{C_{bat}} i_{ESS} \tag{30}$$

where $i_L$ is the converter inductor current, and $i_{ESS}$ represents the battery current. For designing the ISMC, a procedure similar to the DC-link voltage control presented in the previous section is followed, thereby it is not repeated here.

By following a procedure similar to that used in (23) to (29), the final control law for generating the reference charging current in CV mode is obtained as:

$$i_{CV}^{*} = k_2 i_L - C_{bat}\dot{V}_{ESS,ref} + C_{bat}\lambda_2 \tilde{V}_{ESS} + (C_{bat}\eta + (1 - k_2)|i_L|)sign(s) \tag{31}$$

**Designing ISMC for CC Charging Mode (E2G & G2E)**

In this operating mode, the DC/DC converter performs fast bidirectional charging and discharging between the grid and the ESS. The objective of designing the ISMC in this case is to achieve accurate and fast tracking of the ESS current based on the reference powers $P_{G2E}^{*}$ and $P_{E2G}^{*}$. For designing the desired SMC, Equation (5) is considered, and by applying minor modifications, Equation (32) is derived.

$$\frac{di_{ESS}}{dt} = \frac{-1}{L_{bat}} V_{ESS} + \frac{1}{L_{bat}} g.V_{dc} \tag{32}$$

where $V_{ESS}$ denotes the battery voltage, $V_{dc}$ is the DC bus voltage. According to the companion model presented in (12), the following variable transformations are performed:

$$x = i_{ESS} \tag{33}$$

$$f = \frac{-1}{L_{bat}} V_{ESS} \tag{34}$$

$$u = \frac{1}{L_{bat}} g.V_{dc} \tag{35}$$

Again, inspired by the earlier design method and by considering an integral sliding surface similar to (16), the ISMC for ESS current tracking is designed in the following steps:

By setting $\dot{s} = 0$, the final control input is obtained as:

$$\begin{aligned} \hat{u}_{eq} &= -\hat{f} + \dot{x}_d - \lambda_3 \tilde{x} \\ u &= \hat{u}_{eq} - ksign(s) \end{aligned} \tag{36}$$

where:

$$\hat{f} = -\frac{k_3 V_{ESS}}{L_{bat}} \tag{37}$$

and $0 < k_3 < 1$.

By applying the convergence condition in (19) to ensure the exponential stability of the proposed controller, we have

$$s\dot{s} \leq -\eta|s| \leq (F-k)|s| \Rightarrow k > F + \eta \tag{38}$$

where the function *F* is defined by the following relation:

$$F \triangleq \frac{|1-k_3|}{L_{bat}} V_{ESS} \tag{39}$$

According to (36), the reference control signal $\Delta i_{ESS}$ is expressed in (40), which is directly fed into the HCC block.

$$\begin{aligned} \Delta i_{ESS} = -k_3 V_{ESS} + L_{bat} \cdot i_{ESS-ref} - \lambda_3 L_{bat} \tilde{\imath}_{ESS} - (\eta L_{bat} + |1-k_3| V_{ESS}) \\ \cdot sign(s) \end{aligned} \tag{40}$$

where $\tilde{\imath}_{ESS} = i_{ESS} - i_{ESS-ref}$.

## PROPOSED ISMC BASED CONTROLLERS FOR DC/AC CONVERTER

The control of power flow between the utility grid and the DC-link of the DC/DC converter is handled by the bidirectional DC/AC converter. When this converter is connected to the power grid, it runs in grid-following mode to control both active and reactive power. When the grid is disconnected, the converter must run in grid-forming mode to supply the AC side loads from the ESS by controlling voltage and frequency. Here, the goal of designing the SMC is to achieve accurate tracking of the dq-axis current components on the grid side. To design the ISMC, Equations (8) and (9) are considered, which are then slightly modified and rewritten as

$$\frac{di_{fd}}{dt} = -\frac{R_f}{L_f} i_{fd} - \omega_g i_{fq} - \frac{1}{L_f} v_{gd} + \frac{v_{id}}{L_f} \tag{41}$$

$$\frac{di_{fq}}{dt} = -\frac{R_f}{L_f} i_{fq} + \omega_g i_{fd} - \frac{1}{L_f} v_{gq} + \frac{v_{iq}}{L_f} \tag{42}$$

To simplify the design and analysis, the following variable transformations are applied:

$$\begin{cases} \begin{bmatrix} x_1 \\ x_2 \end{bmatrix} = \begin{bmatrix} i_{fd} \\ i_{fq} \end{bmatrix}, \begin{bmatrix} u_1 \\ u_2 \end{bmatrix} = \begin{bmatrix} v_{id} \\ v_{iq} \end{bmatrix} \\ a_1 = \dfrac{R_f}{L_f}, \quad a_2 = \dfrac{v_{gd}}{L_f}, \quad a_3 = \dfrac{v_{gq}}{L_f}, \quad b = \dfrac{1}{L_f} \end{cases} \tag{43}$$

By considering (41)–(43), the companion model is obtained as:

$$\begin{cases} \dot{x}_1 = f_1 + bu_1, & y_1 = x_1 \\ \dot{x}_2 = f_2 + bu_2, & y_2 = x_2 \end{cases} \tag{44}$$

The functions $f_1$ and $f_2$ are defined by the following relations:

$$\begin{cases} f_1 \triangleq -a_1 x_1 - \omega_g x_2 - a_2 \\ f_2 \triangleq -a_1 x_2 + \omega_g x_1 - a_3 \end{cases} \tag{45}$$

while the system parameter constraints and uncertainties are modeled by the following constraints:

$$\begin{cases} a_1^{min} \le a_1 \le a_1^{max} \\ a_2^{min} \le a_2 \le a_2^{max} \\ a_3^{min} \le a_3 \le a_3^{max} \\ b_{min} \le b \le b_{max} \end{cases} \tag{46}$$

The parameters presented in (43) are functions of the fundamental quantities of the equivalent circuit of the real system i.e., $v_{gd}$, $v_{gq}$, $R_f$ and $L_f$. Therefore, the values of these quantities lie within specific, physically bounded ranges. For example, the parameter $a_1 = \frac{R_f}{L_f}$, depends on the two key quantities $R_f$ and $L_f$, each of which, in practice, may vary within the ranges $0.01 \le R_f \le 0.1\,\Omega$ and $1 \le L_f \le 5\,\text{mH}$. Consequently, the parameter $a_1$ can be restricted to the interval $10 \le a_1 \le 20$, ensuring that a bounded input yields a bounded output. The same procedure is applied to determine the admissible ranges of the other parameters, namely $a_2$, $a_3$ and $b$.

Two integral sliding surfaces for the dq-axis currents are defined as

$$s_d = e_d + \lambda_d \int e_d \, dt \tag{47}$$

$$s_q = e_q + \lambda_q \int e_q \, dt \tag{48}$$

where $e_d = y_d - y_d^*$ and $e_q = y_q - y_q^*$ represent the tracking errors for dq-axis currents ($i_{fd}$, $i_{fq}$), and $\lambda_d, \lambda_q$ are positive control gains that shape the convergence dynamics.

**Designing ISMC for Tracking d-Axis Current**

To obtain the control rule for the input $u_1$, the error dynamics of the output variable $y_d$ are initially analyzed. The time derivative of this error is calculated as

$$\dot{e}_d = \dot{y}_d - \dot{y}_d^* = \dot{x}_1 - \dot{y}_d^* = f_1 - \dot{y}_d^* + bu_1 \tag{49}$$

Incorporating this into the sliding surface dynamics in (53), its derivative is achieved by

$$\dot{s}_d = \dot{e}_d + \lambda_d e_d = f_1 + \lambda_d e_d - \dot{y}_d^* + bu_1 \tag{50}$$

To satisfy the sliding condition with exponential convergence, both sides of (50) are multiplied by $s_d$, yielding

$$\begin{aligned} s_d\dot{s}_d &= s_d(f_1 + \lambda_d e_d - \dot{y}_d^*) + sbu_1 \\ &\leq |s_d|\left|f_1 - \hat{f}_1 + \hat{f}_1 + \lambda_d e_d - \dot{y}_d^*\right| + sbu_1 \end{aligned} \tag{51}$$

Using the triangle inequality and factoring out $b|s_1|$, we have

$$s_d\dot{s}_d \leq b|s_d|\left(\frac{\left|f_1 - \hat{f}_1\right|}{b} + \frac{\left|\hat{f}_1 + \lambda_d e_d - \dot{y}_d^*\right|}{b} + \frac{s_d}{|s_d|}u_1\right) \leq -b\eta_d|s_d| \tag{52}$$

Here, $b$ is conservatively replaced with its minimum value $b_{min}$ from the parameter set. Thus, the control action for $u_1$ is obtained as

$$u_1 = \left(-b_{min}\eta_d - \frac{F_1 + \left|\hat{f}_1 + \lambda_d e_d - \dot{y}_d^*\right|}{b_{min}}\right) sign(s_d) \tag{53}$$

In this relation, the function $\hat{f}_1$ is estimated as

$$\hat{f}_1 = -\alpha_{1ave}x_1 - \omega_g x_2 - a_{2ave} \tag{54}$$

where $a_{2ave} = \left(a_2^{min} + a_2^{max}\right)/2$ and $a_{1ave} = \left(a_1^{min} + a_1^{max}\right)/2$.

The bound on the modeling uncertainty is

$$\left|f_1 - \hat{f}_1\right| \leq |(a_1 - \alpha_{1ave})x_1 + (a_2 - a_{2ave})| \leq \alpha_{1ave}|x_1| + a_{2ave} \tag{55}$$

which, the function $F_1$ is defined as

$$F_1 = \alpha_{1ave}|x_1| + a_{2ave} \tag{56}$$

To mitigate the chattering phenomena often associated with discontinuous control rules, the sign function presented in (53) can be replaced with a continuous approximation, such as the function which previously introduced in (24).

**Designing ISMC for Tracking q-Axis Current**

To design the SMC for regulating the q-axis current $i_{fq}$, a similar procedure to the d-axis control design is utilized. Therefore, the sliding surface defined in (48) and the output $y_q$ are applied to formulate the control input $u_2$. The error dynamics related to $y_q$ is given as:

$$\dot{e}_q = \dot{y}_q - \dot{y}_q^* = \dot{x}_2 - \dot{y}_q^* = f_2 - \dot{y}_q^* + bu_2 \tag{57}$$

Integrating the error $e_q$ into the sliding surface given in (48), the time derivative is calculated as:

$$\dot{s}_q = \dot{e}_q + \lambda_q e_q = f_2 + \lambda_q e_q - \dot{y}_q^* + bu_2 \tag{58}$$

where, $y_q^*$ and $\dot{y}_q^*$ represent the reference current and its time derivative in the q-axis. To ensure exponential convergence to the sliding surface, as presented by the stability condition in (19), both sides of (58) are multiplied by $s_q$, yielding:

$$\begin{aligned} s_q\dot{s}_q &= s_q\left(f_2 + \lambda_q e_q - \dot{y}_q^*\right) + sbu_2 \\ &\leq \left|s_q\right|\left|f_2 - \hat{f}_2 + \hat{f}_2 + \lambda_q e_q - \dot{y}_q^*\right| + sbu_2 \end{aligned} \tag{59}$$

Following the same structure as in the d-axis design, the ultimate control law for the q-axis current is given as:

$$u_2 = \left(-b_{min}\eta_q - \frac{F_2 + \left|\hat{f}_2 + \lambda_q e_q - \ddot{y}_q^*\right|}{b_{min}}\right) sign(s_q) \tag{60}$$

The term $\hat{f}_2$ is an estimate of the nonlinear function $f_2$, defined as:

$$\hat{f}_2 = -\alpha_{1ave}x_2 + \omega_g x_1 - a_{3ave} \tag{61}$$

where $a_{3ave} = \left(a_3^{min} + a_3^{max}\right)/2$

To bound the uncertainty between $f_2$ and $\hat{f}_2$, the relation (62) is derived.

$$\left|f_2 - \hat{f}_2\right| \leq |(a_1 - \alpha_{1ave})x_2 + (a_3 - a_{3ave})| \leq \alpha_{1ave}|x_2| + a_{3ave} \tag{62}$$

Thus, the upper bound $F_2$ is defined by:

$$F_2 = \alpha_{1ave}|x_2| + a_{3ave} \tag{63}$$

As in the d-axis controller, chattering can be mitigated by replacing the sign function in (60) with a smooth approximation, such as the saturation function in (24). It is necessary to emphasize that the constants $\lambda_d$ and $\lambda_q$ can be chosen through different tuning methods, like the pole placement strategy.

**Bidirectional DC/AC Grid Following Converter Based on ISMC**

To manage bidirectional power flow between the utility grid and the ESS, the DC/AC converter must run in grid-following mode to achieve synchronization of voltage and frequency with the power grid. For this purpose, a PLL based on the synchronous reference frame, as shown in Figure 8, is employed for frequency synchronization. First, the three-phase grid voltages and currents are transformed into the dq reference frame, resulting in the voltage components $v_{gd}, v_{gq}$ and current components $i_{fd}, i_{fq}$. These signals, along with the current references $i_{fd}^*, i_{fq}^*$ are fed into the ISMC block. This controller was previously designed to track the grid currents $i_{fd}, i_{fq}$.

The d-axis reference current of the controller ($i_{fd}^*$) is used to control the DC-link voltage during E2G and G2E modes. The DC-link voltage controller based on ISMC is designed similarly to the controller developed for the E2L discharge mode in Section (Designing ISMC for Discharging Mode (E2L) and is not repeated here. The reference current for the DC voltage controller is obtained by dividing the reference powers $P_{E2G}^*$ and $P_{G2E}^*$ by the voltage $V_{ESS}$. To maintain a unity power factor at the PCC bus, the q-axis current of the DC/AC converter controller is set to zero.

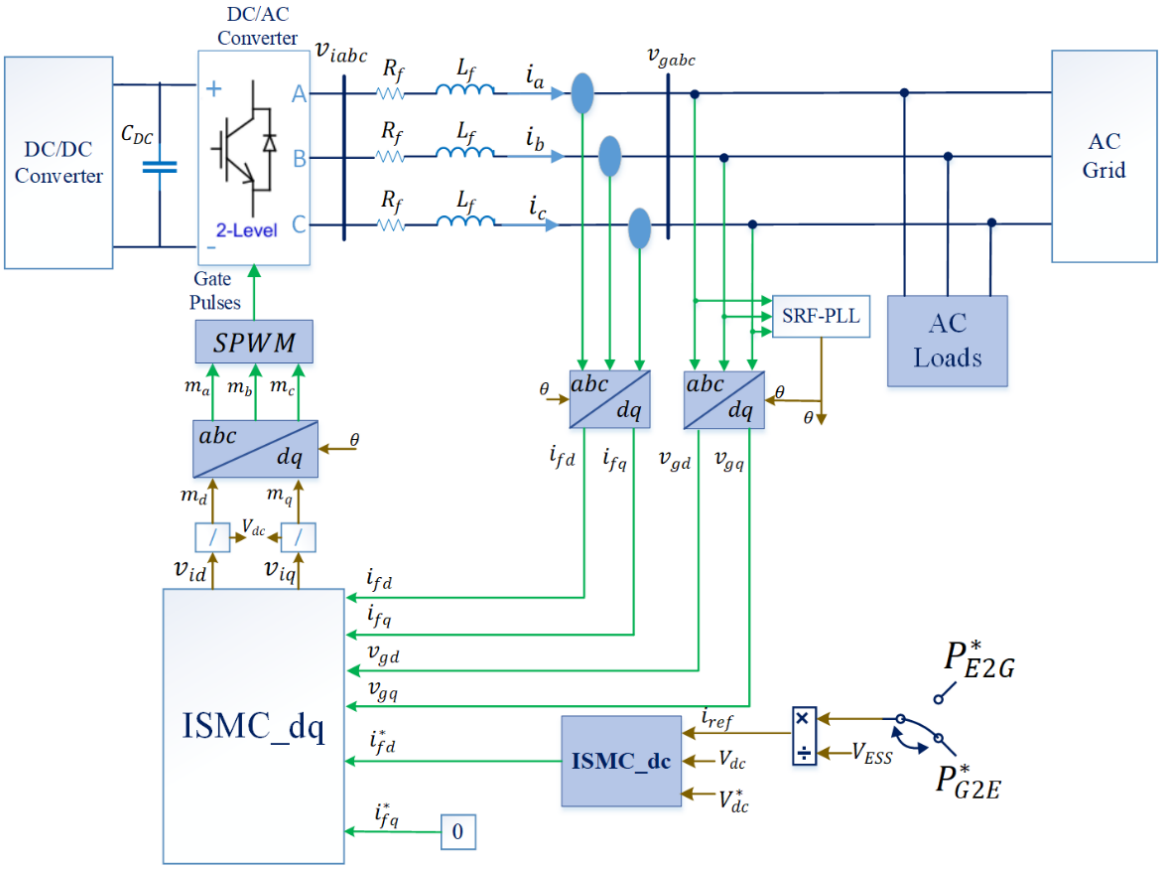


**Figure 8.** Block diagram of ISMC based DC/AC grid-following converter.

**Bidirectional DC/AC Grid Forming Converter Based on ISMC and Droop**

When the fast-charging system is disconnected from the power grid, the ESS must supply not only the DC side loads but also the AC side loads. In this case, the DC/AC converter operates in grid-forming mode to regulate the voltage and frequency across the AC loads. The proposed controller structure, based on ISMC and droop control, is shown in Figure 9. In this scheme, an ISMC is designed to track the load terminal voltages in the synchronous reference frame ($v_{gd}, v_{gq}$). The reference voltage for the d-axis ($v^*_{gd}$) is obtained using the droop controller defined in (64). The q-axis reference voltage ($v^*_{gq}$) is set to zero, as expressed in (65).

$$v^*_{gd} = V_0 - n(Q - Q_{ref}) \tag{64}$$

$$v^*_{gq} = 0 \tag{65}$$

Here, $V_0$ is the reference voltage of the load's fundamental component, $n$ is the voltage droop coefficient, $Q$ is the measured reactive power, and $Q_{ref}$ is the reference reactive power of the load.

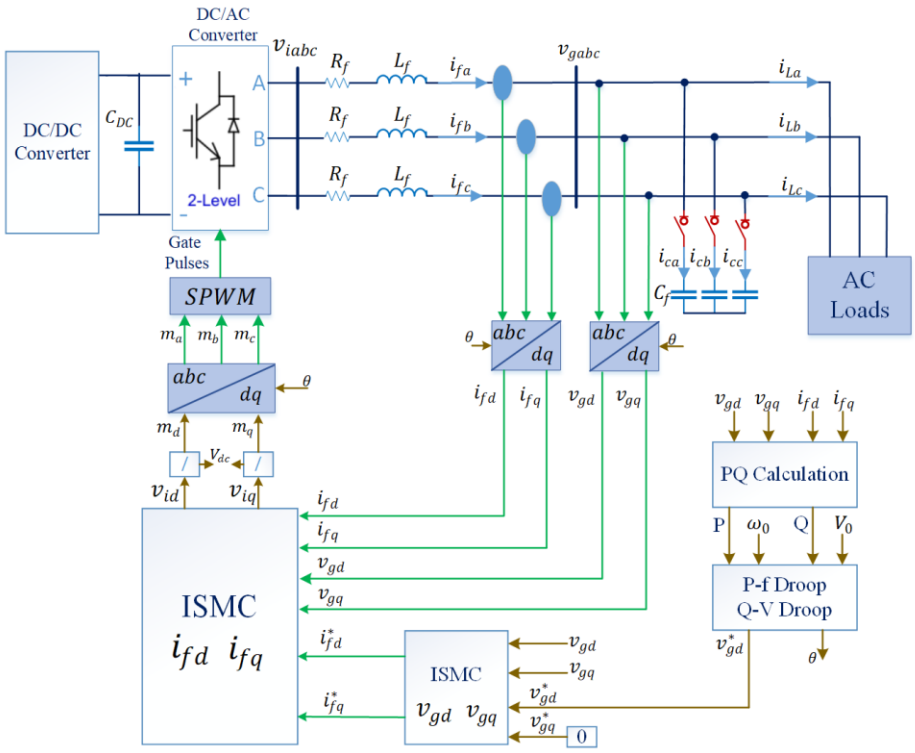


**Figure 9.** Block diagram of ISMC based DC/AC grid-forming converter when grid is disconnected.

To regulate the frequency of the load bus, frequency droop control is applied according to (66) to generate the synchronization angle $\theta$ required for Park transformations.

$$\begin{cases} \omega_g = \omega_0 - m(P - P_{ref}) \\ \theta = \int \omega dt \end{cases} \tag{66}$$

In this relation, $\omega_0$ is the reference frequency of the load, $m$ is the frequency droop coefficient, $P$ is the measured active power, and $P_{ref}$ is the reference active power of the load.

The load reference currents ($i_{fd}^*, i_{fq}^*$) are generated as outputs from the ISMC voltage controller block In E2L mode, the DC/AC converter supplies RL loads through the ESS, and the parallel filter capacitors ( $C_f$ ) are connected, as illustrated in Figure 9, to work with the series RL filter and compensate for switching harmonics. To design the sliding mode voltage controllers, the voltage–current equations of the system considering a second-order RLC filter are written as

$$\begin{cases} \dfrac{dv_{gd}}{dt} = -\omega L_f v_{gq} - \dfrac{1}{C_f} i_{Ld} + \dfrac{1}{C_f} i_{fd} \\ \dfrac{dv_{gq}}{dt} = \omega L_f v_{gd} - \dfrac{1}{C_f} i_{Lq} + \dfrac{1}{C_f} i_{fq} \end{cases} \tag{67}$$

where $i_{Ld}$ , $i_{Lq}$ are the dq-axis currents of the load. To obtain the companion model and design the integral sliding mode voltage controller, the following variable transformations are applied:

$$\begin{bmatrix} x_1 \\ x_2 \end{bmatrix} = \begin{bmatrix} v_{gd} \\ v_{gq} \end{bmatrix}, \quad \begin{bmatrix} u_1 \\ u_2 \end{bmatrix} = \begin{bmatrix} i_{fd} \\ i_{fq} \end{bmatrix}, \quad Z_f = \omega_g L_f, \quad \alpha = \frac{1}{C_f} \tag{68}$$

By substituting the variable changes from (68) into (67), we obtain:

$$\begin{cases}\dot{x}_1 = -Z_f x_2 - \alpha i_{Ld} + \alpha u_1 \\ \dot{x}_2 = Z_f x_1 - \alpha i_{Lq} + \alpha u_2\end{cases} \tag{69}$$

According to (69), the functions $f_1$ and $f_2$ can be defined as

$$\begin{cases}f_1 \triangleq -Z_f x_2 - \alpha i_{Ld} \\ f_2 \triangleq Z_f x_1 - \alpha i_{Lq}\end{cases} \tag{70}$$

The constraints of the above system are defined by

$$\begin{cases}Z_f^{min} < Z_f < Z_f^{max} \\ \alpha_{min} < \alpha < \alpha_{max}\end{cases} \tag{71}$$

The integral sliding surfaces for controlling the load voltages in the dq axes are given by

$$\begin{cases}s_{vd} = e_{vd} + \lambda_{vd} \int e_{vd} dt \\ s_{vq} = e_{vq} + \lambda_{vq} \int e_{vq} dt\end{cases} \tag{72}$$

Here, $\lambda_{vd}$ and $\lambda_{vq}$ are positive design constants, and $e_{vd}$ and $e_{vq}$ represent the voltage control errors defined by

$$\begin{cases}e_{vd} = v_{gd} - v_{gd}^* \\ e_{vq} = v_{gq} - v_{gq}^*\end{cases} \tag{73}$$

The time derivatives of the voltage errors are given by

$$\begin{cases}\dot{e}_{vd} = \dot{v}_{gd} - \dot{v}_{gd}^* = \dot{x}_1 - \dot{v}_{gd}^* = f_1 - \dot{v}_{gd}^* + \alpha u_1 \\ \dot{e}_{vq} = \dot{v}_{gq} - \dot{v}_{gq}^* = \dot{x}_2 - \dot{v}_{gq}^* = f_2 - \dot{v}_{gq}^* + \alpha u_2\end{cases} \tag{74}$$

The time derivatives of the sliding surfaces in (72) are calculated as (75) considering (74).

$$\begin{cases}\dot{s}_{vd} = \dot{e}_{vd} + \lambda_{vd} e_{vd} = f_1 + \lambda_{vd} e_{vd} - \dot{v}_{gd}^* + \alpha u_1 \\ \dot{s}_{vq} = \dot{e}_{vq} + \lambda_{vq} e_{vq} = f_2 + \lambda_{vq} e_{vq} - \dot{v}_{gq}^* + \alpha u_2\end{cases} \tag{75}$$

The exponential stability conditions for the sliding surfaces are expressed by the following inequalities

$$\begin{cases}s_{vd}\dot{s}_{vd} \le \alpha|s_{vd}|\left[\dfrac{|f_1 - \hat{f}_1|}{\alpha} + \dfrac{|f_1 + \lambda_{vd} e_{vd} - \dot{v}_{gd}^*|}{\alpha} + \dfrac{s_{vd}}{|s_{vd}|}u_1\right] \le -\alpha\eta_{vd}|s_{vd}| \\ s_{vq}\dot{s}_{vq} \le \alpha|s_{vq}|\left[\dfrac{|f_2 - \hat{f}_2|}{\alpha} + \dfrac{|f_2 + \lambda_{vq} e_{vq} - \dot{v}_{gq}^*|}{\alpha} + \dfrac{s_{vq}}{|s_{vq}|}u_2\right] \le -\alpha\eta_{vq}|s_{vq}|\end{cases} \tag{76}$$

Finally, the control signals $u_1$ and $u_2$, representing the reference currents $i_{fd}^*$ and $i_{fq}^*$, are obtained as shown by

$$\begin{cases}u_1 = \left[-\alpha_{min}\eta_{vd} - \dfrac{F_1 + |\hat{f}_1 + \lambda_{vd} e_{vd} - \dot{v}_{gd}^*|}{\alpha_{min}}\right] sign(s_{vd}) \\ u_2 = \left[-\alpha_{min}\eta_{vq} - \dfrac{F_2 + |\hat{f}_2 + \lambda_{vq} e_{vq} - \dot{v}_{gq}^*|}{\alpha_{min}}\right] sign(s_{vq})\end{cases} \tag{77}$$

The estimated functions $\hat{f}_1$ and $\hat{f}_2$ are presented by

$$\begin{cases}\hat{f}_1 = -\dfrac{Z_f}{2} x_2 - \alpha_{avg} i_{Ld} \\ \hat{f}_2 = \dfrac{Z_f}{2} x_1 - \alpha_{avg} i_{Lq}\end{cases} \tag{78}$$

Additionally, the functions $F_1$ and $F_2$ are written by

$$\begin{cases} F_1 \triangleq \dfrac{Z_f}{2}|x_2| \\ F_2 \triangleq \dfrac{Z_f}{2}|x_1| \end{cases} \tag{79}$$

## PERFORMANCE EVALUATION

To evaluate the performance and verify the effectiveness of the proposed bidirectional fast-charging system based on DC/DC and DC/AC converters controlled by ISMC, extensive simulations are performed in MATLAB/Simulink. Figure 2 is considered as the reference for the simulation studies. Various scenarios are presented to demonstrate the impact and capability of the designed control methods, including: (a) Bidirectional power flow under grid-connected mode: In the ESS charging mode (G2E), the operating mode determination algorithm of the DC/DC converter activates the fast current charging (CC) mode and the slow voltage charging (CV) mode accordingly. Additionally, the DC/AC converter runs in grid-following mode to control power based on the reference power commands. Under these conditions, in addition to charging the ESS batteries, the utility grid can also supply the DC and AC side loads. In the E2G, only the discharging mode is activated, allowing the ESS to transfer power to system loads and deliver excess power back to the utility grid. (b) Grid outage and load supply by ESS (E2L): Under this condition, the utility grid is completely disconnected, and the ESS is solely responsible for supplying all system loads. Therefore, the proposed algorithm sets the DC/DC converter to DC-link voltage control mode, while the DC/AC converter operates in grid-forming mode to regulate the voltage and frequency of the AC side loads. A droop-based voltage and frequency controller is employed for this purpose. The key simulation parameters are presented in Table 2. The parameters listed in this table are directly applied in the simulation results shown in Figures 4–9, including DC-link voltage regulation, current responses, and mode-transition behavior.

**Table 2.** System and control parameters used in simulation studies.

| Parameters | Value |
|---|---|
| Grid nominal Line-Line voltage and frequency ($v_g, f_g$) | 380 v, 50 Hz |
| RLC filter parameters ($R_f, L_f, C_f$) | 0.5 Ω, 2 mH, 50μF |
| DC-link nominal voltage and capacitance ($V_{dc}, C_{dc}$) | 750 v, 10 mF |
| Nominal voltage and capacity of ESS ($V_{ESS}, C_{ESS}$) | 640 v, 6.3 A. h |
| Inductance of DC/DC buck-boost converter ($L_{bat}$) | 10 mH |
| Switching frequency of DC/AC converter ($f_{sw}$) | 20 kHz |
| Sample time ($T_s$) | 1 μs |
| ISMC parameters for DC voltage ($\lambda_{dc}, \eta_{dc}$) | 3000, 2000 |
| ISMC parameters for dq-currents ($\lambda_{dq}, \eta_{dq}$) | 0.5, 1.5 |
| ISMC parameters for ESS current (CC_mode) ($\lambda_{i_{ESS}}, \eta_{i_{ESS}}$) | 0.1, 0.4 |
| ISMC parameters for ESS voltage (CV_mode) ($\lambda_{v_{ESS}}, \eta_{v_{ESS}}$) | 1000, 400 |
| ISMC parameters for voltages controllers (E2L mode) ($\lambda_{v_{dq}}, \eta_{v_{dq}}$) | 1.5, 1 |
| ISMC parameters for currents controllers (E2L mode) ($\lambda_{i_{dq}}, \eta_{i_{dq}}$) | 10, 15 |
| Frequency droop control coefficient ($m$) | $10^{-7}$ (rad/s/w) |
| Voltage droop control coefficient ($n$) | $10^{-4}$ (v/var) |

The control system is implemented in the discrete domain with a sampling time of 1 μs, while the power converter is operated at a fixed switching frequency of 20 kHz using PWM modulation. Unless otherwise stated, the simulations assume ideal voltage and current sensing, with no measurement noise, quantization effects, or analogue-to-digital conversion resolution limits. In addition, controller computation delay and PWM actuation delay are not explicitly modeled. These assumptions allow an assessment of the intrinsic dynamic capability of the proposed control strategy under idealized conditions.

Switching losses are not included in the simulation model, as the primary goal of this study is to evaluate the control performance and dynamic behavior of the proposed strategy. This assumption allows a clear comparison of different controllers under identical operating conditions without the influence of device-specific loss parameters.

**Simulation of G2E and E2G Operation Modes during Fixed Loads**

In this scenario, the performance of the proposed bidirectional fast-charging system based on SMC is examined under G2E and E2G conditions, while the load profile of the system stays constant. The reference powers of the DC/DC converter controller ( $P_{E2G}^{*}, P_{G2E}^{*}$ ) vary across different intervals, forming a dynamic power profile. This results in bidirectional power flow between the grid and the ESS, while simultaneously supplying the AC and DC loads. Figure 10 illustrates the simulation details related to the system's performance during successive charging and discharging operations of the ESS. Figure 10a shows the DC-link voltage. Despite power flow changes, the voltage stays at 750 V, with only minor fluctuations occurring at the moments of disturbance. The variations in power transfer by the ESS during charging (G2E) and discharging (E2G) modes through the DC/DC converter are shown in Figure 10b. It is evident that during each time interval, the ESS power closely follows its corresponding reference command and accurately matches the predefined power values. The active power exchanged between the utility grid and the DC/AC converter is presented in Figure 10. Positive active power indicates power flowing from the utility grid toward the AC loads and the DC/AC converter. Conversely, negative active power indicates surplus energy generated by the ESS being delivered to the grid. The SOC of the ESS is also shown in Figure 10d. A negative slope of the SOC curve indicates ESS discharging, while a positive slope reflects fast charging operation in CC mode. The initial SOC of the ESS is assumed to be 60% in this simulation. The charging and discharging currents of the ESS ($i_{ESS}$) are depicted in Figure 10e, which in each interval precisely follow the ESS current reference.

A positive current indicates the discharging state of the ESS, while a negative current corresponds to the fast-charging operation in CC mode. Figure 10f presents the active and reactive power consumed by the AC and DC loads of the system. The constant power of the DC load is 3 kW. The active and reactive powers of the AC loads are 5 kW and 1 kVAr,

respectively. The reactive power of the AC load ($Q_L$) is entirely supplied by the reactive power of the utility grid ($Q_g$).

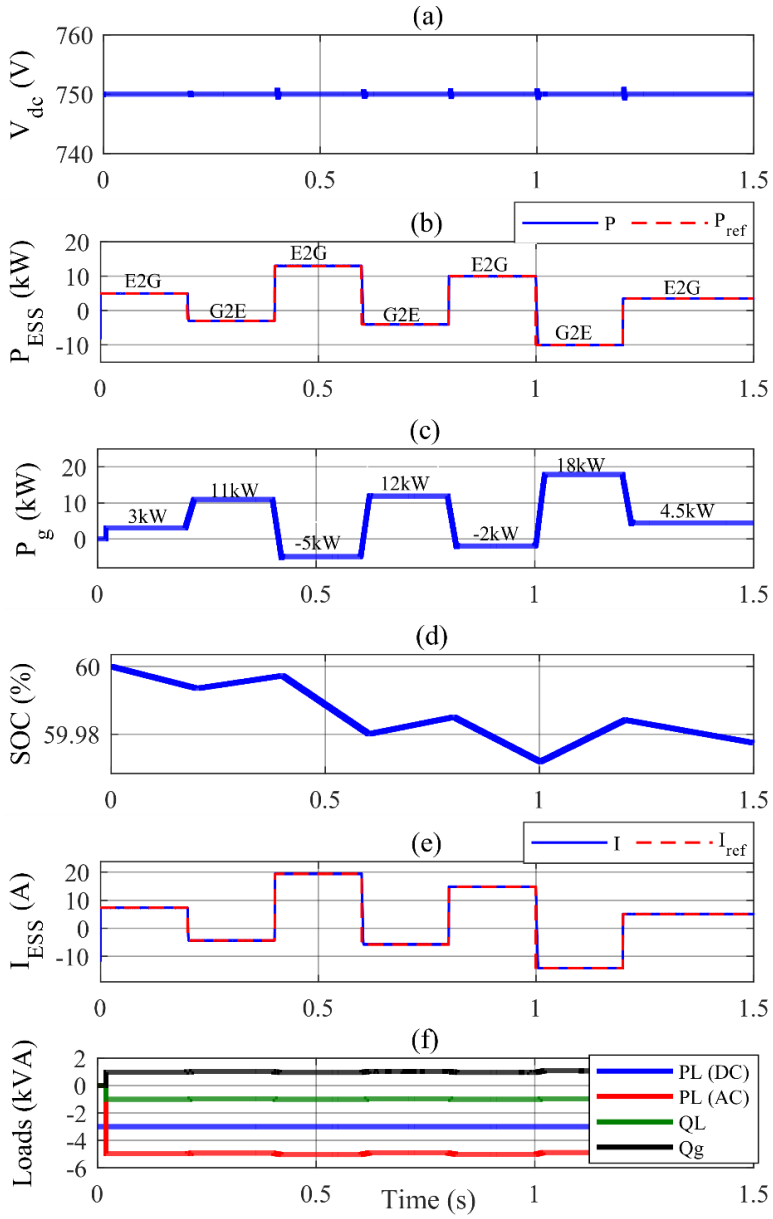


**Figure 10.** Simulation results of bidirectional fast-charging system during G2E and E2G operation modes, (**a**) DC-link voltage, (**b**) ESS power, (**c**) grid active power, (**d**) ESS battery's SOC, (**e**) ESS current, (**f**) active and reactive powers of loads.

The total active load of the system (DC load + AC load) is 8 kW. In the time interval from 0 to 0.2 s, the ESS delivers 5 kW to the system based on its reference power. Out of this, 3 kW is used to supply the local DC load, and the remaining 2 kW is transferred by the DC/AC converter to the AC side. This 2 kW is added to 3 kW received from the grid to supply the total 5 kW AC load. This relationship is reflected in Figure 10b,c. As another example, consider the time interval between 0.4 and 0.6 seconds. In this period, the ESS generates 13 kW of power according to its reference. With this generated power, the ESS supplies the AC and DC loads totaling 8 kW,

and the remaining 5 kW is delivered back to the utility grid. In all other time intervals, this balance of power transfer between sources and loads is maintained.

The performance of the ISMC current controllers on the AC side of the DC/AC converter is shown in Figure 11. As shown in Figure 11a, the three-phase voltage waveforms at the PCC bus ($v_{pcc}$) remain stable and free of harmonic distortion under power disturbances. The peak phase voltage amplitude at the PCC ($v_{m,ph}$) is 311 V. The three-phase currents at the PCC bus ($i_{pcc}$), under varying system operating modes and bidirectional power flow changes, are presented in Figure 11b. It is to be noted that in the final time interval (1.2 s to 1.5 s), the amplitude of the three-phase PCC currents is nearly zero. This indicates that the algebraic sum of generated and consumed power in the system is balanced, resulting in zero net active power at the PCC during that period. Accurate and fast dynamic tracking of the d- and q-axis current components ($i_{fd}^{*}$ و $i_{fq}^{*}$) at the PCC bus by the ISMC is shown in Figure 11c,d, respectively. The zero value of the reactive current ($i_{fq}$) in Figure 11d confirms the realization of a unity power factor at the PCC.

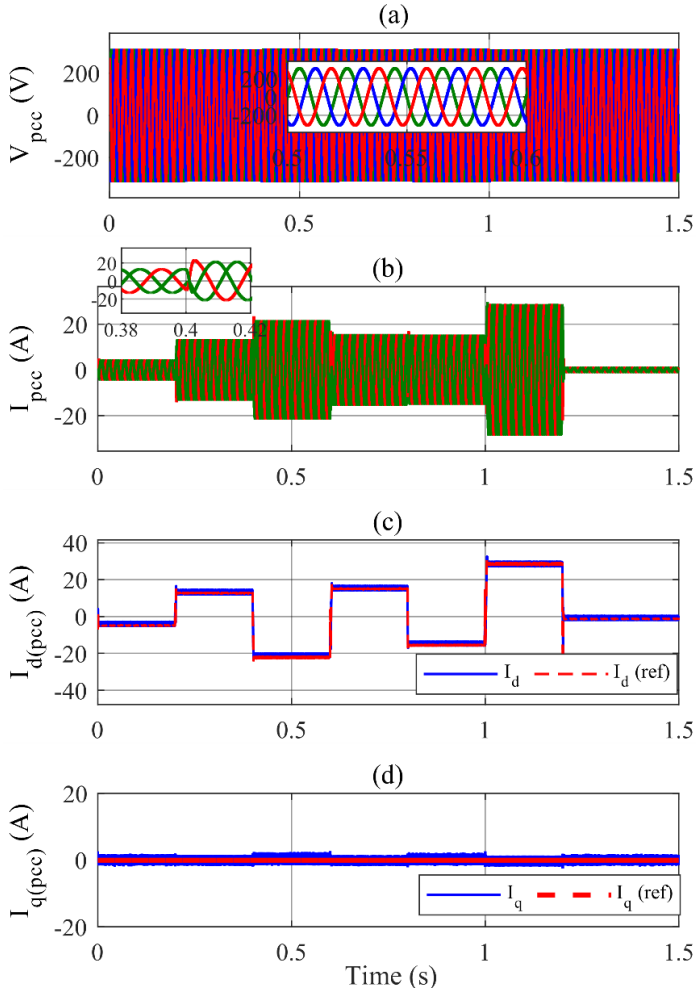


**Figure 11.** Performance of AC side controllers during G2E and E2G operation modes, (**a**) Three phase voltages of PCC, (**b**) three phase currents of PCC, (**c**) d-axis current of PCC, (**d**) q-axis current of PCC.

The performance of the SMC, including their sliding surfaces and control errors during the E2G and G2E operating conditions, is shown in Figure 12. As seen in Figure 12a,b, the sliding surface and control error for the DC-link voltage controller tend toward zero with sharp transient state because of the fast dynamics convergence. This demonstrates that the system state trajectories rapidly converge to the sliding surface ($s_{dc}$).

The sliding surface of the current controller for the d-axis component ($s_d$), along with the current tracking error ($e_d$), converges to zero in the steady state as illustrated in Figure 12c,d. However, during current direction changes, relatively large but momentary overshoots and undershoots are observed. These can be attributed to the fast exponential convergence characteristics of the sliding mode. The sliding surface of the current controller for the q-axis component ($s_q$), and its corresponding tracking error, as shown in Figure 12e,f, consistently converge to zero without any significant oscillations under all operating conditions.

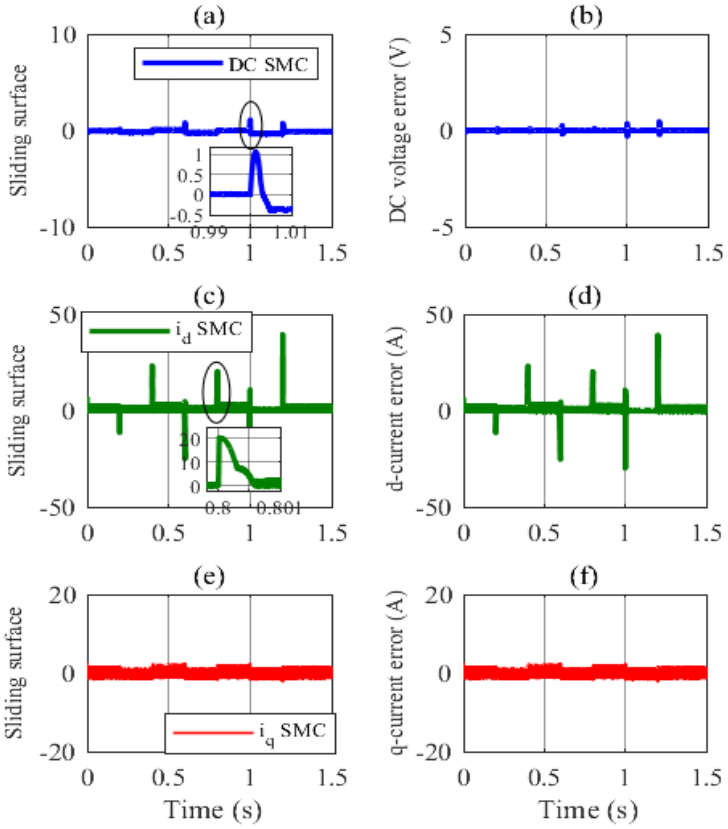


**Figure 12.** Sliding surfaces and errors of controllers during E2G and G2E modes, (**a**) DC controller sliding surface, (**b**) DC voltage error, (**c**) d-axis current controller sliding surface, (**d**) d-axis current error, (**e**) q-axis current controller sliding surface, (**f**) q-axis current error.

### Simulation of G2E and E2G Operation Modes during Loads Variation

In this scenario, the variations in the active and reactive load profiles are examined during periods of constant ESS charging and discharging power. The results of this section are illustrated in Figures 13 and 14. The step changes in the active power of the AC and DC loads are shown in

Figure 13a, which initially increase and then decrease over different time intervals. The maximum total AC and DC load occurs during the time interval between 0.6 and 0.9 s, reaching 13 kW. Figure 13b presents the reactive power profile of the AC side loads ($Q_L$), which is subsequently supplied by the utility grid ($Q_L$). Since the reactive power reference for the DC/AC converter is set to zero, the converter does not contribute to supplying the reactive power demand of the loads.

The reference charging power of the ESS in the G2E mode ($P^*_{G2E}$) is fixed at −7 kW, as shown on the left side of Figure 13c. Therefore, the utility grid must not only supply the system loads but also charge the ESS. This condition is depicted on the left side of Figure 13d. The results show that during all time intervals of load variation, the active power injected by the utility grid remains positive. In this case, the total power supplied by the utility grid is the sum of the load demand and the ESS charging power. The maximum power injected by the utility grid occurs between 0.6 and 0.9 s, reaching 20 kW (i.e., 13 kW for supplying the loads and 7 kW for charging the ESS).

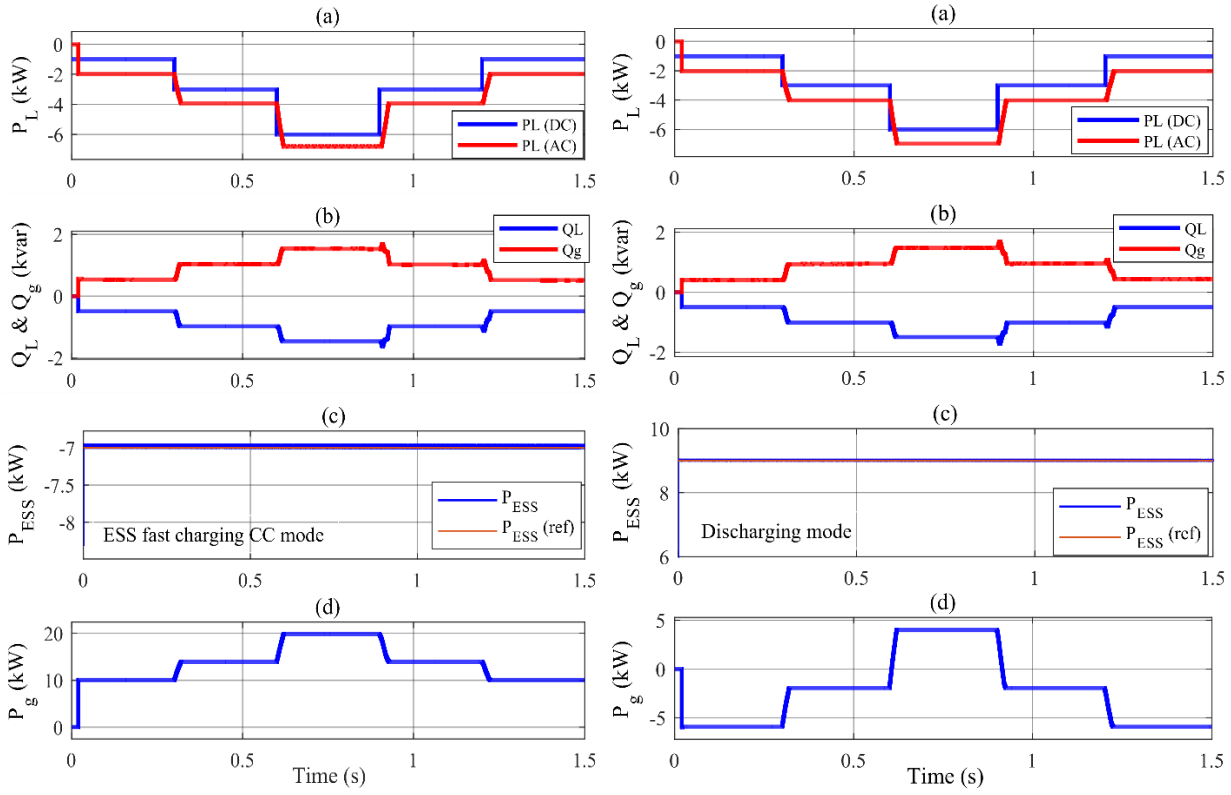


**Figure 13.** Simulation results related to G2E and E2G modes during loads variation for ESS charging mode (left-hand) and discharging mode (right-hand). (**a**) DC and AC load active power, (**b**) reactive powers of load and grid, (**c**) ESS power, (**d**) grid power.

The reference discharge power of the ESS in the E2G mode ($P^*_{E2G}$) is fixed at +9 kW, as shown on the right side of Figure 13c. In this mode, the system load is supplied jointly by the utility grid and the ESS. The right side of Figure 13d illustrates the power profile exchanged between the utility grid

and the fast-charging system. According to this figure, during intervals where the grid power ($P_g$) is negative, it indicates that excess power from the ESS is being fed back into the utility grid. Only during the time interval between 0.6 and 0.9 s—when the system load reaches its maximum value (13 kW)—the ESS alone is not sufficient to meet the demand, and an additional +4 kW of power is supplied by the utility grid.

Other key parameters obtained from the simulation of this scenario are presented in Figure 14. As shown, the DC-link voltage of the converters is regulated by the proposed ISMC during both charging and discharging modes, remaining stable at the reference value of 750 V across all time intervals with oscillations below 0.5% (Figure 14a). The three-phase sinusoidal currents at the PCC ($i_{pcc}$), depicted in the left panel of Figure 14b, exhibit a step increase in amplitude up to 0.9 s, followed by a gradual decrease until the end of the simulation under the CC charging mode. In contrast, as shown on the right side of Figure 14b, during the discharging mode, the amplitude of the three-phase sinusoidal currents at the PCC initially decreases in line with the step load increase until 0.9 s, then begins to rise again.

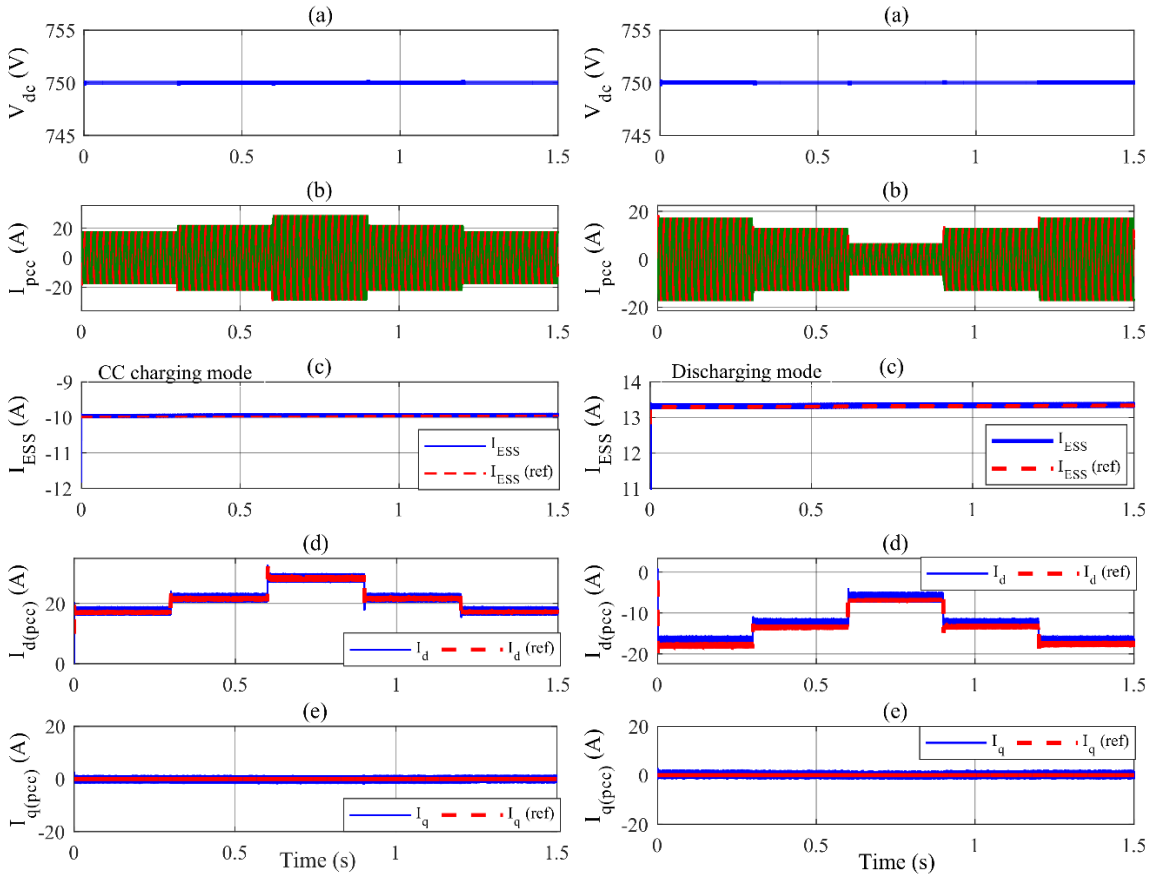


**Figure 14.** AC side controllers' performance during loads variation for variation for ESS charging mode (left-hand) and discharging mode (right-hand). **(a)** DC-link voltage, **(b)** three phase currents of PCC, (c) ESS current, **(d)** d-axis current of PCC, **(e)** q-axis current of PCC.

According to the left panel of Figure 14c, the ESS current ($i_{ESS}$) in charging mode is -10 A, and in discharging mode, shown in the right panel, it is +13.3 A. In both cases, the ESS current of $i_{ESS}$ closely follows its reference values. Figure 14d,e respectively show the d- and q-axis current components of the sliding mode current controllers ($i_{fd}, i_{fq}$) during ESS charging and discharging modes, and it is evident that these current components also accurately track their respective references.

### Simulation Results in CV Mode

The proposed charging control algorithm illustrated in Figure 7 operates such that, upon the battery SOC reaching 80%, the charging mode automatically transitions from CC mode to CV mode. This ensures the batteries are subsequently charged with a significantly lower current than that of the fast-charging phase. The simulation results of this scenario are presented in Figure 15. Figure 15a shows the ESS battery voltage ($V_{ESS}$) during both the CC and CV charging modes. It is observed that immediately after switching from CC to CV mode, the battery voltage $V_{ESS}$ drops from 735 V (in CC) to a predetermined 696 V (in CV), and the SMC designed for the CV mode effectively performs accurate and rapid voltage tracking.

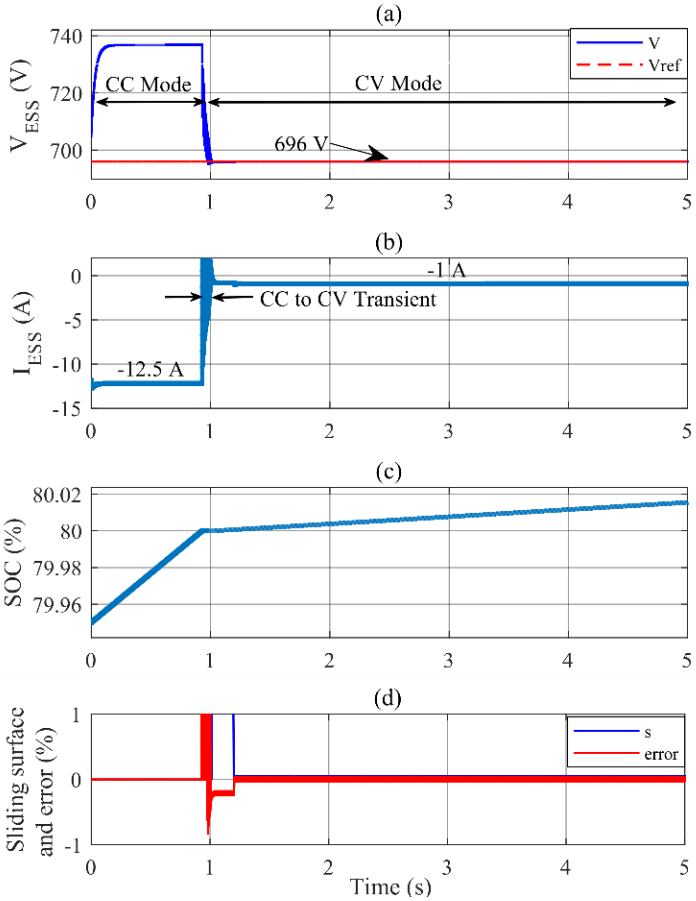


**Figure 15.** Simulation results related to transition between CC and CV charging mode of ESS. (**a**) ESS voltage, (**b**) ESS current, (**c**) ESS SOC, (**d**) sliding surface and error of ESS voltage controller in percent.

According to Figure 15b, the battery charging current, $i_{ESS}$ decreases from 12.5 A to 1 A after the mode transition. A short transient occurs in the battery current at the moment of switching modes, which, due to its brevity, can be considered negligible in terms of adverse effects. Figure 15c displays the SOC of the ESS batteries in both CC and CV modes, clearly indicating a reduction in the charging rate after transitioning to the CV mode. The sliding surface of the ESS voltage controller, along with the voltage tracking error, is shown in Figure 15d. It is evident that upon activation of the CV mode, both parameters converge toward zero, indicating precise voltage tracking by the proposed ISMC-based controller.

**Simulation Results of E2L Mode for Grid-Forming DC/AC Converter**

When the power grid is disconnected from the bidirectional fast-charging system, in order to maintain power supply to the system loads, the DC/AC converter must operate in grid-forming mode to regulate the voltage and frequency of the AC side loads. Under these conditions, the ESS should enter the E2L mode and supply both DC and AC loads. A frequency droop controller can adjust the load-side frequency according to the active power demanded by the loads. Similarly, to maintain the load voltage at its nominal value, a voltage droop controller can regulate the load voltage by considering the reactive power required by the loads. The proposed mode control algorithm sets the DC/DC converter to operate in DC-link voltage regulation mode. Figure 16a shows the DC-link voltage. The ISMC-based controller maintains the voltage at 750 V without deviation, even under frequent load variations.

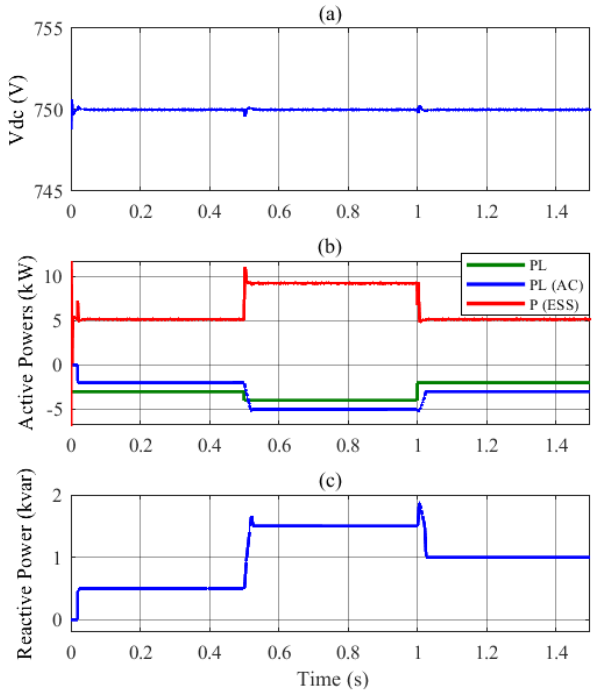


**Figure 16.** Simulation results for E2L operation mode during load changes. **(a)** DC-link voltage, **(b)** active powers of loads and ESS, **(c)** reactive power of load.

The profile of the active power consumed by the loads and generated by the ESS is presented in Figure 16b. It is observed that, in each time interval, the total power consumed by the loads is equal to the power generated. Figure 16c shows the profile of the reactive power absorbed by the AC load. The performance of the outer voltage and frequency controllers based on ISMC and droop during E2L mode and under load variations is illustrated in Figure 17. The three-phase voltages at the PCC bus ($v_{pcc}$) are shown in Figure 17a. The phase voltages are regulated with a peak amplitude of 310 V, are purely sinusoidal, and exhibit no significant harmonic distortion. Figure 17b shows the RMS values of the PCC phase voltages ($v_{rms}$), indicating that all three phases follow the nominal reference value of 220 V. The d-axis voltage component of the PCC bus ($v_{gd}$), regulated by the ISMC, precisely tracks the reference value of 310 V, which is obtained from the droop controller, as shown in Figure 17c. As expected, the q-axis voltage component of the PCC bus ($v_{gq}$) remains at its reference value of zero, as illustrated in Figure 17d. The frequency variations at the PCC bus ($f$) under dynamic changes in AC load are presented in Figure 17e. It is clearly observed that the droop frequency controller successfully maintains the bus frequency at its nominal value of 50 Hz despite active power fluctuations in the AC load.

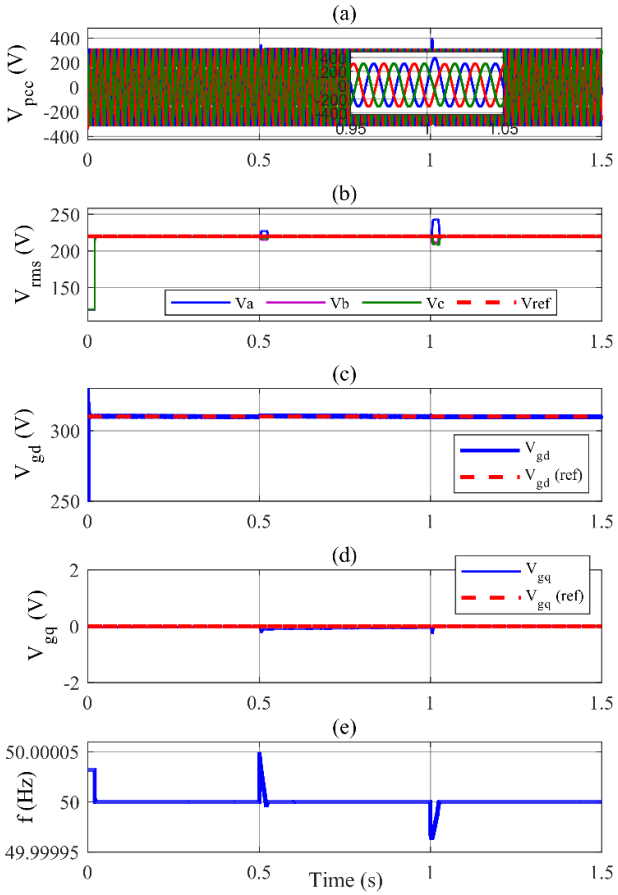


**Figure 17.** Performance of voltage and frequency controllers based on ISMC and droop in E2L mode. (**a**) Three phase voltage of PCC, (**b**) RMS phase voltages of PCC, (**c**) d-axis voltage of PCC, (**d**) q-axis voltage of PCC, (**e**) PCC bus frequency.

Figure 18 illustrates the performance of the inner current controllers of the charging system in grid-forming and E2L modes during load variations. The three-phase currents of the PCC bus ($i_{pcc}$) are shown in Figure 18a. The amplitude of the three-phase currents changes according to the AC load variation profile. The total harmonic distortion (THD) of the AC load currents is only 1.2%. Figure 18b,c presents the d-axis and q-axis current components of the inner controllers of the DC/AC converter ($i_{gd}$, $i_{gq}$), which precisely follow their reference signals. The switching effect of the load on the dq currents of the DC/AC converter is evident, with instantaneous overshoot and undershoot occurring at t = 0.5 s and t = 1 s, respectively. The discharging current of the ESS ($i_{ESS}$), supplying the system loads, is depicted in Figure 18d, which closely follows its reference signal.

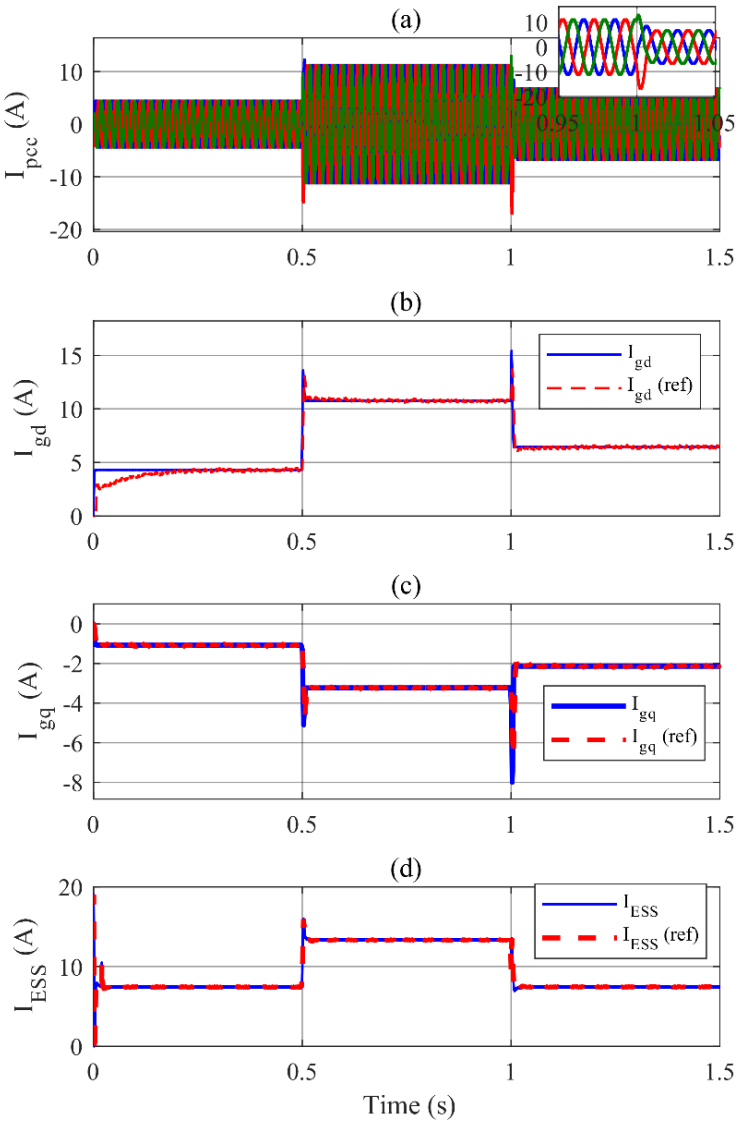


**Figure 18.** Performance of inner current controllers in E2L mode during load changes. (**a**) Three phase currents of PCC, (**b**) d-axis current of PCC, (**c**) q-axis current of PCC, (**d**) ESS current.

**Comparative Results**

Figure 19 presents the comparative results of three control strategies—PI, ADRC, and the proposed ISMC—on system performance during active power reference changes across four key outputs: The DC bus voltage ($V_{dc}$), three-phase currents of the PCC ($I_{pcc}$), d-axis current of the converter ($I_d$), and the q-axis current of the converter ($I_q$). The DC voltage response of the system shows significant differences between the control strategies as illustrated in Figure 19a. The PI controller (blue curve) exhibits considerable overshoot (0.4%) and settling time (50ms), particularly near $t$ = 0.6 to 0.64s, as shown in the inset. The ADRC (red curve) shows reduced overshoot (0.3%) and settling time (40 ms) but its steady state response has a significant error. In contrast, the ISMC (black curve) demonstrates the most stable behavior, maintaining the voltage near the desired value with negligible overshoot and settling time. It should be emphasized that these values correspond to ideal simulation conditions and should not be interpreted as hardware-level performance. The key outcome is the comparative improvement achieved by the proposed method rather than the absolute numerical magnitude of the transient indices. The current response of phase 'a' also highlights the performance differences. The PI controller again shows large oscillations and instability, particularly during the transient period at the beginning of the time range. The ADRC significantly reduces these oscillations, providing a smoother current waveform. However, the DC voltage response does not follow the reference voltage of 750 V during steady state, especially in the interval of 0s to 0.6s. The ISMC, however, achieves the smoothest and most stable current profile, minimizing the oscillation levels, particularly in the steady-state condition (Figure 19b).

According to Figure 19c, the PCC current in the direct axis ($i_d$) shows a rapid rise with a large peak in both the PI and ADRC strategies. The PI strategy exhibits pronounced oscillations, especially in the early time interval. The ADRC shows some improvement but still struggles with oscillatory behavior. On the other hand, the ISMC provides a steady and smooth response, as demonstrated by the black curve, which shows negligible oscillations after the initial response and effectively stabilizes the current value. Also, due to Figure 19d, the PCC quadrature current ($i_q$) shows similar trends, where the PI controller introduces large oscillations, while the ADRC reduces them but still displays some fluctuations. The ISMC achieves the most stable and smooth response, particularly in eliminating steady-state oscillations and ensuring minimal deviation from the desired value. Table 3 lists the PI and ADRC tuning parameters. PI gains are typical values for grid-connected 750 V DC-link voltage controllers tuned via pole-placement. For designing the ADRC parameters ($b_0$, $\omega_0$, $\omega_c$) the ESO bandwidth is selected 5 times higher than controller bandwidth. The ISMC tuning parameters are shown in Table 2. Quantitative performance comparison of the controllers is listed in Table 4. The PI controller typically produces higher overshoot and settling time indices

due to weak robustness under parameter variation. ADRC improves dynamics and reduces IAE/RMSE compared to PI, but still introduces higher overshoot and settling time. ISMC provides the lowest THD, lowest steady-state error, and almost zero overshoot compared to two other controllers.

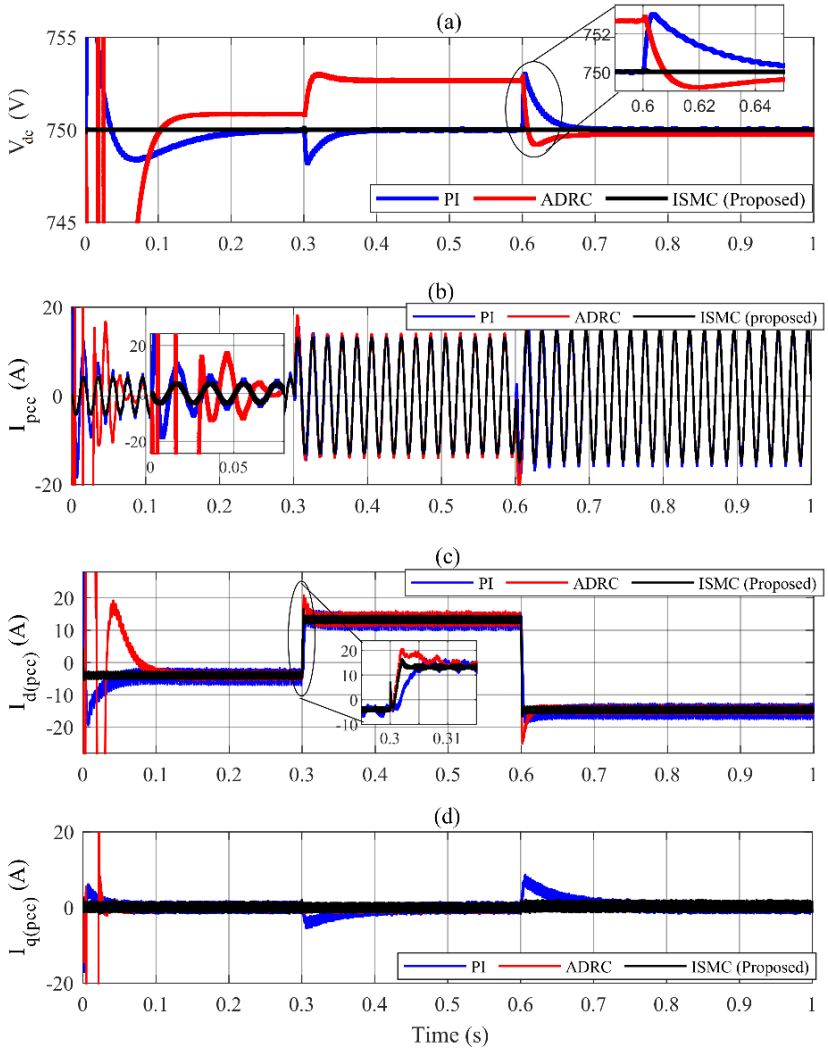


**Figure 19.** Comparative results between the proposed ISMC, PI, and ADRC methods. (**a**) DC link voltage, (**b**) PCC current of phase "a", (**c**) d-axis current of PCC, (**d**) q-axis current of PCC.

**Table 3.** Controller tuning parameters.

| Controller | $k_p$ | $k_i$ | $b_0$ | $\omega_0(rad/s)$ | $\omega_c(rad/s)$ |
|---|---|---|---|---|---|
| PI (DC voltage) | 10 | 400 | – | – | – |
| PI (dq-currents) | 5 | 100 | – | – | – |
| ADRC (DC voltage) | – | – | 157 | 1500 | 400 |
| ADRC (d-current) | – | – | 157 | 4000 | 350 |
| ADRC (q-current) | – | – | 157 | 10000 | 350 |

**Table 4.** Quantitative performance comparison.

| Controller | THD of Grid Current (%) | IAE (V·s) | RMSE of $V_{dc}$ (V) | Overshoot (%) | Settling Time (ms) |
|---|---|---|---|---|---|
| PI | 4.96% | 135 | 10 | 0.4 | 50 |
| ADRC | 4.06% | 80 | 7 | 0.3 | 40 |
| ISMC (Proposed) | 0.48% | 30 | 3 | 0.001 | 0.01 |

The results clearly indicate that the ISMC strategy outperforms the PI and ADRC controllers in all aspects, particularly in terms of minimizing overshoot, oscillations, and settling time. This demonstrates the superior robustness and efficiency of the proposed ISMC strategy in controlling the system. While the PI controller is simpler, it struggles with stability and performance in comparison. The ADRC provides a balance but still cannot match the performance of the ISMC, especially in the steady-state condition.

In practical implementations, switching losses contribute to efficiency reduction and semiconductor temperature rise. Since all controllers considered in this study operate at the same switching frequency and employ the same converter topology, the exclusion of switching losses does not affect the relative performance comparison. Moreover, the proposed controller does not increase switching frequency or switching transitions and therefore, is not expected to impose additional switching loss or thermal burden compared to conventional methods.

**Harmonic analysis**

The harmonic analysis of the PCC current in the time interval 0.4 s < t < 0.5 s with PI, ADRC, and the proposed ISMC is illustrated in Figure 20. Under identical conditions and based on phase-a current waveforms shown in Figure 19b, the THD of the PCC phase-a current for the PI, ADRC, and proposed ISMC is 4.96, 4.06, and 0.48%, respectively. These values are presented in Figure 20a–c, respectively. It is clearly observed that with the use of the robust proposed ISMC method, the PCC current THD is significantly improved compared to the other two approaches.

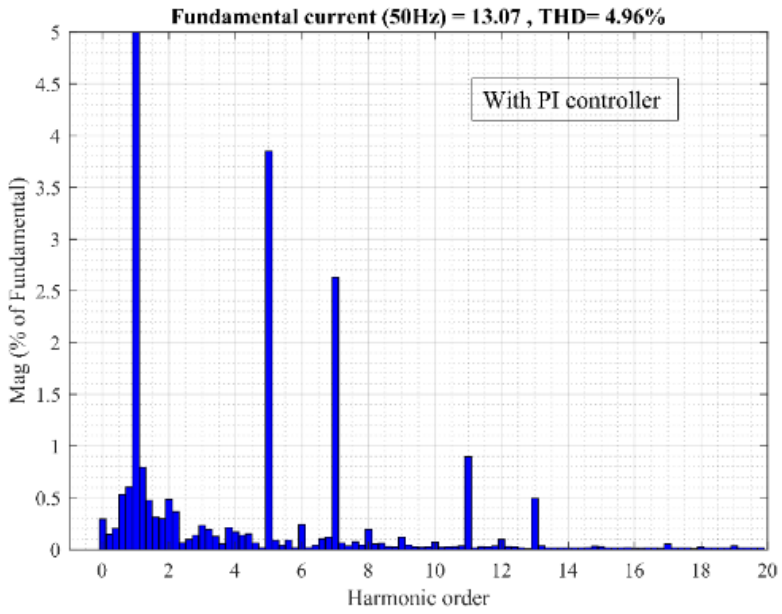


**(a)**

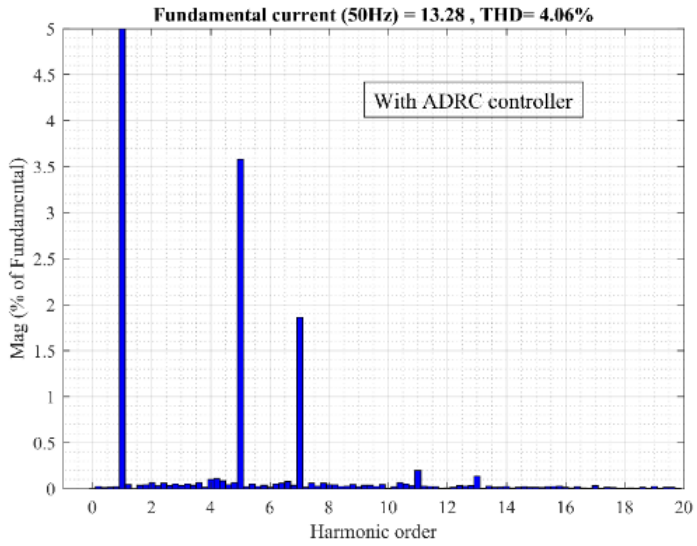


**(b)**

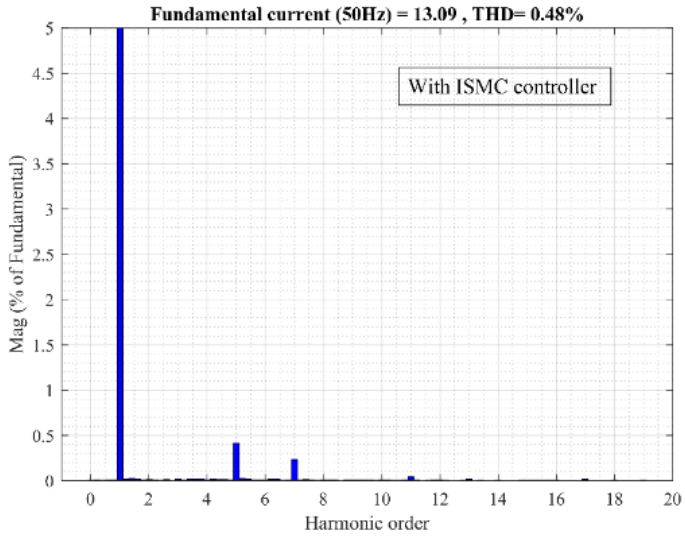


**(c)**

**Figure 20.** Harmonic spectrum of PCC current in the interval 0.4 < t< 0.5 s. (**a**) PI, (**b**) ADRC, (**c**) Proposed ISMC.

### Sensitivity Analysis

To evaluate the robustness of the proposed ISMC, a sensitivity analysis was conducted on the DC-link voltage control loop under realistic operating conditions for the fast charger. The DC-link nominal voltage was set to 750 V, and the switching frequency to 20 kHz. According to common charger specifications, the allowable ripple magnitude for the DC-link capacitor should not exceed 2% of the nominal value, i.e., $\Delta V_{dc,max} = 0.02 \times 750 = 15$ V.

The ISMC parameters ($\lambda_1$, $k_1$ and the boundary-layer thickness $\phi$) were tuned such that the steady-state ripple remains well below this limit while maintaining a fast transient response. The controller's robustness was assessed by varying the dominant DC-link dynamic parameter $a_{nom} = 1/C_{dc}$ in (11) by $\pm 30\%$ around its nominal value, representing typical

variations in effective DC-link capacitance and load conditions. Three cases were simulated: $a = 0.7a_{nom}$, $a = a_{nom}$, $a = 1.3a_{nom}$.

The resulting DC-link voltage responses are shown in Figure 21. All trajectories exhibit a rapid rise to the 750 V reference within approximately 6–8 ms, consistent with practical fast charger dynamics. Once the sliding motion is established, the responses for all three uncertainty cases nearly overlap, indicating low sensitivity of the closed-loop system to parameter deviations. Importantly, the steady-state ripple remains within the 2% (15 V) design constraint for all cases, demonstrating that the boundary-layer implementation of the sliding function effectively suppresses high-frequency chattering and ensures a smooth steady-state waveform suitable for hardware realization.

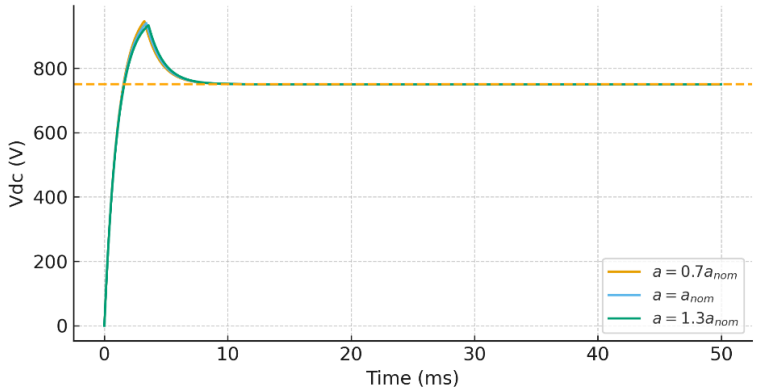


**Figure 21.** Sensitivity analysis of DC voltage.

### Switching between Grid-Following and Grid-Forming Modes

In this section, the dynamic transition between grid-following and grid-forming operating modes is simulated and analyzed. The switching between grid-following and grid-forming modes can be performed either manually or through a power management algorithm. In this analysis, during the time interval $0 \le t \le 0.5$ s, the charging system operates in grid-following control mode while connected to the power grid. At $t = 0.5$ s, the system is disconnected from the grid and transitions to grid-forming control. Subsequently, at $t = 0.75$ s, the system is reconnected to the power grid, and the DC/AC converter control mode returns to grid-following. The results of these transitions are presented and discussed in detail in Figures 22–24.

Stability during mode switching is ensured by maintaining identical inner-loop dynamics in both grid-following and grid-forming modes. The switching action affects only the outer-loop reference generation, while the closed-loop poles of the inner control system remain unchanged. As a result, the overall system avoids pole migration across the stability boundary during the transition, leading to a stable and well-damped transient response. Therefore, the smooth evolution of DC-link voltage and current responses under load and reference changes indirectly confirms the absence of instability or discontinuity during mode switching.

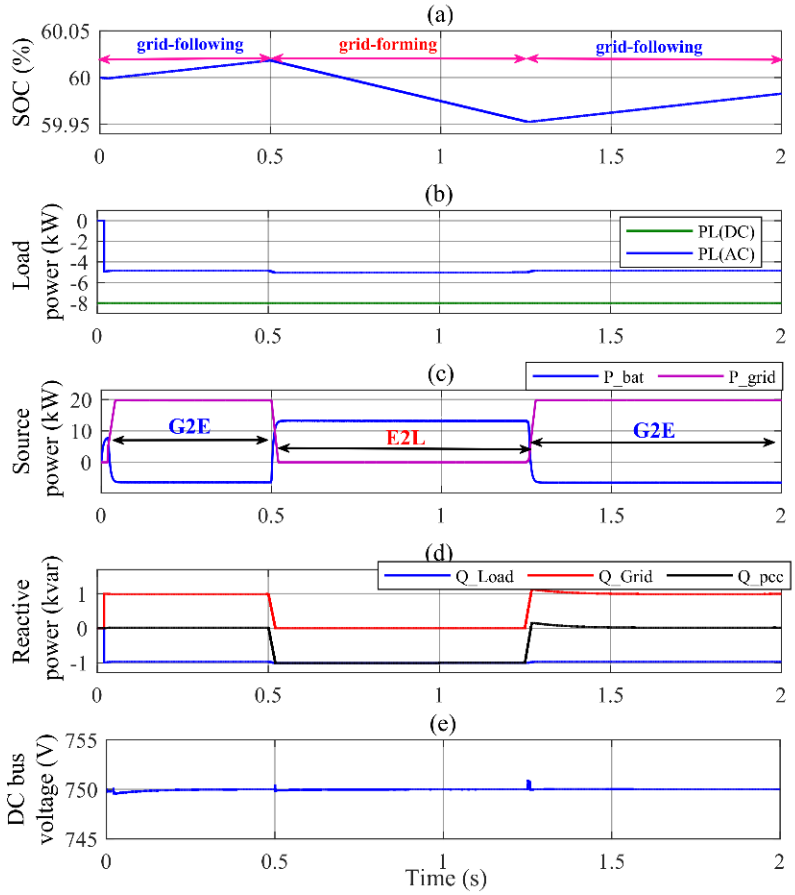


**Figure 22.** Performance of fast-charging system during switching between grid-following and grid-forming modes. (**a**) battery SOC, (**b**) load powers, (**c**) sources powers, (**d**) reactive powers of system, (**e**) DC bus voltage.

The performance of the charging system under changes in the converter operating mode is illustrated in Figure 22 to analyze power distribution. Figure 22a shows the battery charging status under different operating modes. In the first interval, when the converter is connected to the grid, the battery is charged and the system loads are supplied by the power grid. As shown in Figure 22b, the total AC and DC load demand of the system remains constant at 13 kW. During the first interval, when the G2E mode is active, in addition to supplying the 13-kW system load, the battery is charged at a constant power of 7 kW, as depicted in Figure 22c. A very smooth and seamless mode transition between grid-following and grid-forming occurs at t = 0.5 s in both active and reactive power responses. A similar smooth transition is observed at t = 0.75 s, when the converter switches back from grid-forming to grid-following mode. In the first and third intervals, where the converter operates in G2E mode, the reactive power demand of the load is fully supplied by the grid, and the charging system does not participate in reactive power support since it operates at unity power factor. In the second interval, when the converter is disconnected from the grid and operates in grid-forming mode, the DC/AC converter supplies the entire reactive power demand of the load, as shown in Figure 22d. According to Figure 22e, the DC bus voltage remains close to

its nominal value throughout the mode-transition process, exhibiting an overshoot of less than 1%.

Figure 23 illustrates the dynamic and steady-state performance of the converter voltage and frequency under repeated transitions between grid-connected and islanded operating modes. Figure 23a shows the three-phase sinusoidal PCC voltages during the mode transitions, demonstrating stable steady-state operation and smooth dynamic behavior. The variations in the RMS magnitudes of the three-phase voltages in Figure 23b indicate accurate steady-state tracking and a smooth, well-damped dynamic response during the mode transition in the second interval when operating in grid-forming mode. The same behavior is observed for the dq-axis voltage components shown in Figure 23c,d. A slight frequency deviation during the mode transitions is observed in Figure 23e, which confirms the correct operation of the droop controller in grid-forming mode.

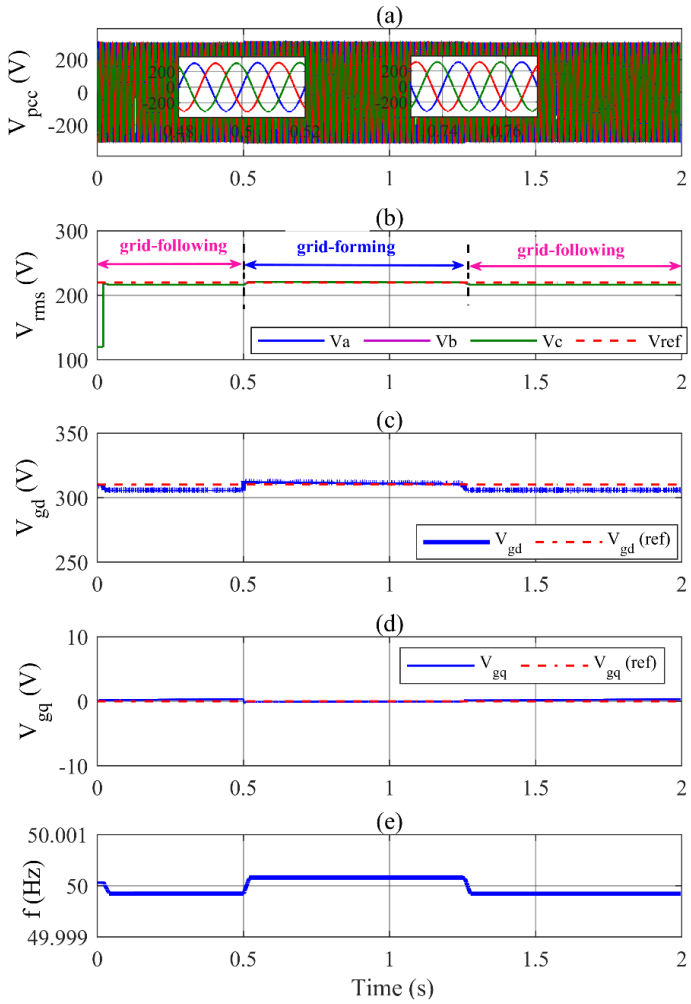


**Figure 23.** Performance of voltage and frequency controllers during switching between grid-following and grid-forming modes. (**a**) Three phase voltage of PCC, (**b**) RMS phase voltages of PCC, (**c**) d-axis voltage of PCC, (**d**) q-axis voltage of PCC, (**e**) PCC bus frequency.

Figure 24 presents the dynamic behavior of the proposed fast-charging system currents during operating mode transitions. The three-phase PCC

currents shown in Figure 24a exhibit smooth and well-damped dynamics across all three operating intervals and remain sinusoidal throughout the mode transitions. In the second interval, corresponding to grid-forming mode, the charging system operates in islanded mode; therefore, the PCC current magnitude matches the AC side load current. Figure 24b demonstrates accurate tracking of the DC/AC converter d-axis current reference in both operating modes. A brief dynamic transient with minor oscillations is observed in the d-axis current waveform at $t$ = 0.75 s during the mode transition; however, it is quickly damped, as shown in the enlarged view of Figure 24b. The q-axis current response in Figure 24c indicates that in grid-following mode (G2E charging mode), the q-axis current remains zero due to unity power factor operation. A short-lived disturbance is observed at $t$ = 0.5 s, after which the q-axis reference current is rapidly tracked. Figure 24d illustrates the battery current response, showing precise tracking of its reference. Overall, the battery current exhibits fast, disturbance-free dynamics during the converter mode transitions.

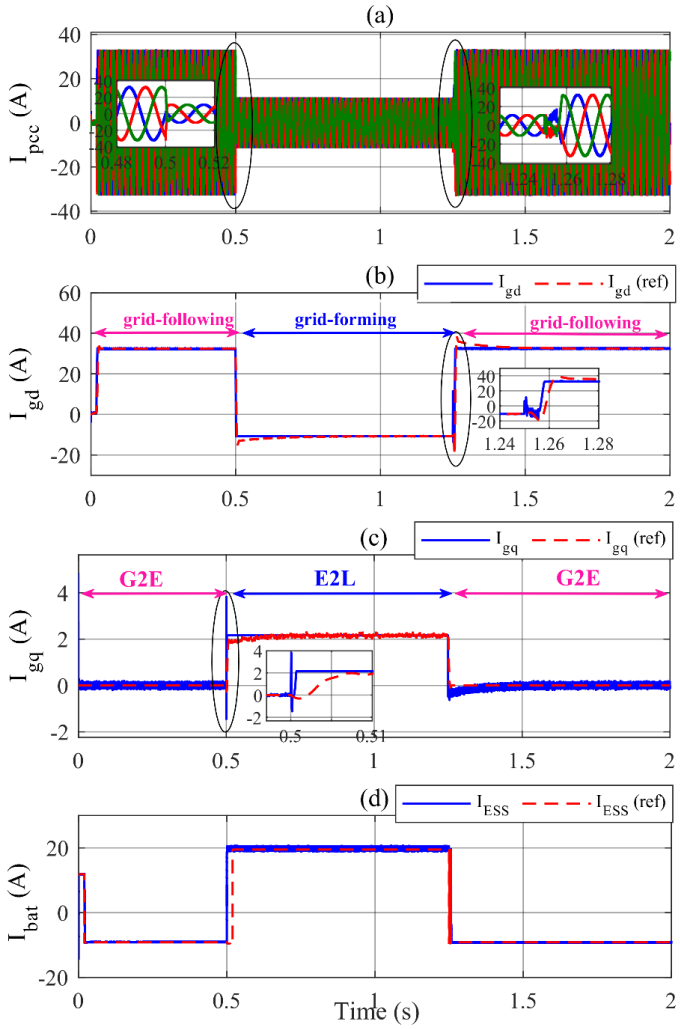


**Figure 24.** Performance of inner current controllers during switching between grid-following and grid-forming modes. **(a)** Three phase currents of PCC, **(b)** d-axis current of PCC, **(c)** q-axis current of PCC, **(d)** battery current.

## CONCLUSIONS

This paper presents a comprehensive design and control framework for a bidirectional fast-charging system for energy storage applications, emphasizing grid-interactive performance and resilience. A dual-stage converter topology, consisting of a bidirectional AC/DC converter and a buck-boost DC/DC converter, is employed to support power flow in both directions between the power grid and the ESS, as well as between the ESS and connected AC/DC loads. To address the inherent challenges of system uncertainties and power disturbances, advanced ISMCs are implemented for both converter stages. The ISMC approach ensures robust voltage and current regulation under varying operating conditions, including grid-connected, grid-support, and grid-forming modes. In particular, the AC/DC converter operates seamlessly in grid-following mode during normal conditions and transitions to grid-forming mode during grid outages, maintaining voltage and frequency regulation to supply critical local AC and DC loads. Additionally, a dynamic power management algorithm is integrated to coordinate the charging and discharging of the battery bank based on real-time SOC and load requirements, enhancing both energy reliability and system efficiency. The proposed system architecture is validated through detailed modeling and simulation, proving its capability in maintaining stable operation, minimizing power quality issues, and offering flexible energy delivery across multiple scenarios. The results affirm that the proposed ISMC-based control strategy outperforms conventional techniques by offering fast transient response, robustness against parameter uncertainties. This makes the system suitable for future smart grid infrastructures, particularly in applications involving high-efficiency, resilient, and intelligent energy storage and delivery systems. Some important findings from this study can be summarized as:

- The proposed ISMC successfully regulates both DC-link voltage and battery voltage under all operating modes, including grid-connected, grid-support, and islanded (grid-forming) conditions. Even under dynamic disturbances and parameter uncertainties, the system maintains voltage and current tracking with minimal steady-state error.
- The proposed system configuration enables bidirectional power flow amongst the grid and ESS and loads during normal operation and grid outages. The transition between modes is smooth and stable, with no overshoot or oscillation in voltage levels.
- The battery charging algorithm, combined with buck-boost DC/DC control, maintains safe charging profiles. Both CC and CV modes are efficiently implemented, maximizing battery health and minimizing charge time.

It is also to be noted that there are still some limitations in real-time implementation including influences of noise, chattering, communication delays, and cost of construction, the impacts and mitigation techniques of which can be considered in future works.

## DATA AVAILABILITY

The dataset of the study is available from the authors upon reasonable request.

## AUTHOR CONTRIBUTIONS

Conceptualization, IS and MRH; methodology, IS; software, MRH; validation, IS, MRH and FS; resources, IS and FS; writing—original draft preparation, IS and MRH.; writing—review and editing, FS; All authors have read and agreed to the published version of the manuscript.

## CONFLICTS OF INTEREST

The authors declare that they have no conflicts of interest.

## FUNDING

No funding was received for conducting this study.

## REFERENCES

1. Kumar Tiwari V, Asim M, Aftab Alam MD, Imran Siddiqui M, Alam MA. Implementation of single-phase shift (SPS) and extended phase shift (EPS) for dual active bridge (DAB). Indian J Sci Technol. 2024;17(41):4262-9. doi: 10.17485/IJST/v17i41.2456
2. Sharma U, Singh B. A bidirectional charging system with the capability to charge electric vehicles with low-voltage powered batteries. Electr Power Syst Res. 2025;243:111501. doi: 10.1016/j.epsr.2025.111501.
3. Panchanathan S, Vishnuram P, Rajamanickam N, Bajaj M, Blazek V, Prokop L, et al. A comprehensive review of the bidirectional converter topologies for the vehicle-to-grid system. Energies. 2023;16(5):2503. doi: 10.3390/en16052503.
4. Pan Z, Chen X, Geng G, Jiang Q. Second harmonic current reduction of dual active bridge converter under dual-phase-shift control in two-stage single-phase inverter for residential energy storage system. J Energy Storage. 2024;103:114158. doi: 10.1016/j.est.2024.114158.
5. Cinik S, Zhao F, De Falco G, Wang X. Efficiency and cost optimization of dual active bridge converter for 350kW DC fast chargers. In: Proceedings of the 2024 Energy Conversion Congress & Expo Europe (ECCE Europe); 2024 Sep 2-6; Darmstadt, Germany. New York (NY, US): IEEE; 2024. p. 1-8. doi: 10.1109/ECCEEurope62508.2024.10751971
6. Wang J, Tan L, Li J, Ji C. Research on model predictive control strategy of three-level dual-active bridge DC-DC converter. Sci Rep. 2025;15:10622. doi: 10.1038/s41598-025-89079-w
7. Sethuraman R, Rudhramoorthy M. Performance of bidirectional on-board charger in electric vehicle: A review. e-Prime Adv Electr Eng Electron Energy. 2024;10:100613. doi: 10.1016/j.prime.2024.100613.

8. Deepak M, Janaki G, Bharatiraja C. Single phase shift dual active bridge high frequency DC-DC converter for electric vehicle battery charger 6.6 kW. In: Proceedings of the 2023 Fifth International Conference on Electrical, Computer and Communication Technologies (ICECCT); 2023 Feb 22-24; Erode, India. New York (NY, US): IEEE; 2023. p. 1-6. doi: 10.1109/ICECCT56650.2023.10179621
9. Kumbhare JM, Kadwane SG. A grid tied solar photovoltaic based off board electric vehicle charger in G2V and V2G mode. AIP Adv. 2024;14(9):095008. doi: 10.1063/5.0212427
10. Muhammetoglu B, Jamil M. Dual active bridge converter with interleaved and parallel operation for electric vehicle charging. Energies. 2024;17(17):4258. doi: 10.3390/en17174258.
11. Shao S, Chen H, Wu X, Zhang J, Sheng K. Circulating current and ZVS-on of a dual active bridge DC-DC converter: A review. IEEE Access. 2019;7:50561-72. doi: 10.1109/ACCESS.2019.2911009.
12. Aparnathi R. Simulation design of three phase grid integrated EV charging station with renewables. J Electr Syst. 2024;20(7s):1625-37. doi: 10.52783/jes.3740
13. Deepti T, Deepa K, Stonier AA, Peter G, Anoop A, Ganji V. Development and efficiency analysis of dual active bridge converter employing SiC devices using TMS 320F280039. IET Circuits Devices Syst. 2025;2025(1):6336609. doi: 10.1049/cds2.6336609
14. Maalandish M, Hosseini SH, Sabahi M, Rostami N, Khooban MH. Soft-switching multiport DC-DC converter for PV/EV applications with a bidirectional port. IET Renew Power Gener. 2024;18(12):1862-79. doi: 10.1049/rpg2.13055.
15. Xuan Y, Yang X, Chen W, Liu T, Hao X. A three-level dual-active-bridge converter with blocking capacitors for bidirectional electric vehicle charger. IEEE Access. 2019;7:173838-47. doi: 10.1109/ACCESS.2019.2957022.
16. Sharma U, Singh B. A bidirectional charger for low-voltage-powered battery vehicles. IEEE Trans Transp Electrif. 2023;9(3):3994-4003. doi: 10.1109/TTE.2023.32376965
17. Li X, Zhang X, Lin F, Sun C, Mao K. Artificial-intelligence-based hybrid extended phase shift modulation for the dual active bridge converter with full ZVS range and optimal efficiency. IEEE J Emerg Sel Top Power Electron. 2023;11(6):5569-81. doi: 10.1109/JESTPE.2022.3185090
18. Rafi MAH, Bauman J. Optimal control of semi-dual active bridge DC/DC converter with wide voltage gain in a fast-charging station with battery energy storage. IEEE Trans Transp Electrif. 2022;8(3):3164-76. doi: 10.1109/TTE.2022.3170737
19. Arogunjo EO, Ojo JO. An insight into the dynamics of a dual active bridge. In: Proceedings of the 2023 IEEE Transportation Electrification Conference & Expo (ITEC); 2023 Jun 21-23; Detroit (MI, US). New York (NY, US): IEEE; 2023. p. 1-6. doi: 10.1109/ITEC55900.2023.10186956

20. Grimm F, Kolahian P, Wood J, Bucknall R, Baghdadi M. An isolated gate driver for multi-active bridges with soft switching. arXiv:2204.01547 [Preprint]. 2022 Apr 4. Available from: https://arxiv.org/abs/2204.01547. Accessed 2026 Feb 26.
21. Aboudrar I, Oubail Y, Boulakhbar M, Ibrahim AW, Ouachtouk I, Alaoui KS. Robust ADRC-controlled bidirectional converters in fast DC BEV charging systems supporting G2V, V2G, and V2H operations. e-Prime Adv Electr Eng Electron Energy. 2025;11:100936. doi: 10.1016/j.prime.2025.100936.
22. Eldali F. Power electronics for distributed energy. In: Rashid MH, editor. Power electronics handbook. 5th ed. Oxford (UK): Butterworth-Heinemann; 2024. p. 977-92. doi: 10.1016/B978-0-323-99216-9.00015-9

How to cite this article:
Soltani I, Reza Hasani M, Shahnia F. Flexible Operation and Control of Bidirectional Chargers Using ISMC for Electric Vehicle Applications. J Sustain Res. 2026;8(1):e260024. https://doi.org/10.20900/jsr20260024.